

Tide-surge interaction in the Pearl River Estuary: a case study of Typhoon Hato

Peng Zheng 1,2 , Ming Li 2 , Caixia Wang 3 , Judith Wolf 4 , Xueen Chen 1 , Michela De Dominicis 4 , Peng Yao 5 , and Zhan Hu 6,7,*

Correspondence*: Zhan Hu

huzh9@mail.sysu.edu.cn

2 ABSTRACT

3

17

19

20

model. The wind field of Typhoon Hato is firstly reconstructed by merging the Holland parametric tropical cyclone model results with the CFSR reanalysis data, which enables the model to reproduce the pure astronomical tides and storm tides well; especially the distinctive oscillation 7 pattern in the measured water levels due to the passage of the typhoon has been captured. Three different types of model runs are conducted in order to separate the water level variations due to the astronomical tide, storm surge and tide-surge interactions in the Pearl River Estuary. 10 Results show the strong tidal modulation of the surge level, as well as alteration of the phase of 11 surge which also changes the peak storm tidal level, in addition to the tidal modulation effects. In order to numerically assess the contributions of three nonlinear processes in the tide-surge 13 interaction and quantify their relative significance, the widely used "subtraction" approach and a 14 new "addition" approach are tested in this study. The widely used "subtraction" approach is found unsuitable for the assessment due to the "rebalance" effect and thus a new "addition" approach 16

In this study, the characteristics and mechanisms of tide-surge interaction in the Pearl River

Estuary (PRE) during Typhoon Hato are studied in detail using a 3D nearshore hydrodynamic

21 Keywords: Tide-Surge Interaction, Pearl River Estuary, Typhoon Hato, FVCOM model, Flood risk, Quadratic bottom friction, Shallow

is proposed with more reasonable test results. Detailed analysis using the "addition" approach

indicates that the quadratic bottom friction, shallow water effect and nonlinear advective effect play the first, second and third most important role in the tidal-surge interaction in the estuary,

2 water effect, Advective effect

respectively.

¹College of Oceanic and Atmospheric Sciences, Ocean University of China, Qingdao, China

²School of Engineering, University of Liverpool, Liverpool, England, United Kingdom

³ Tianjin Binhai New Area Bureau of Meteorology, Binhai New Area, Tianjin, China

⁴National Oceanography Centre, Liverpool, England, United Kingdom

⁵College of Harbor, Coastal and Offshore Engineering, Hohai University, Nanjing, China

⁶School of Marine Science, Sun Yat-sen University, Guangzhou, China

 $^{^7}$ Southern Marine Science and Engineering Guangdong Laboratory (Zhuhai), China

1 INTRODUCTION

Storm surges are abnormal variations of sea level driven by atmospheric forcing associated with extratropical storms or tropical cyclones (also known as hurricanes and typhoons). Combined with the astronomical tide, storm surges often result in extreme water levels and can bring devastating damage to coastal areas, especially for those low-lying areas bordered by extensive continental shelves and exposed to the regular passing of typhoons and storms (Bertin et al., 2012; Zhang et al., 2017). To be able to predict the peak water levels, some operational systems and research studies often superpose an atmospheric-only forced storm surge onto the astronomical tide, without considering the effect of tide-surge interaction (Peng et al., 2004; Bobanović et al., 2006; Graber et al., 2006). However, tide-surge interaction has long been recognised as one of the most important contributors in the storm surges and peak water levels in the coastal regions (Proudman, 1955, 1957; Doodson, 1956; Bernier and Thompson, 2007; Zhang et al., 2010). Comparing with observations, errors in a simple linear superposition of astronomical tide with a separately computed surge are found to be up to 1-2 m (Rego and Li, 2010). Therefore, quantitative insights of tide-surge interaction are very important for the prediction of storm tide level and flood risk assessment.

It has long been recognised that the tide-surge interaction is a nonlinear phenomenon. Previous literature broadly focused on different aspects of the interaction, e.g. the tide-induced modulation of the phase of surge and consequently the variations of sea level; the different contribution from various physical processes to the surge level. Proudman (1955) is among the first few studies to develop solutions for the propagation of an externally forced tide and surge into an estuary of uniform section. It showed that due to tide-surge interaction, the peak storm surge height which occurred near to high tide was less than that which occurred near to low tide for a progressive wave. Rossiter (1961) suggested that a key mechanism of tide-surge interaction was mutual phase alteration, and showed how a negative surge would retard tidal propagation whereas a positive surge would advance the high water. Horsburgh and Wilson (2007) showed that surge generation was reduced during high water and the surge peak was less likely to occur during high water for a large amplitude tide. Rego and Li (2010) studied the effects of tide and shelf geometry under the Hurricane Rita. Results indicated that for landfall at midebb or midflood, the storm tide level was less affected, but for landfall at high tide or low tide, the peak storm tide was either reduced or increased compared to a linear superposition.

It is also widely accepted that the tide-surge interaction is attributed to three nonlinear physical processes: (a) the nonlinear horizontal and vertical advection in the momentum equations (b) the nonlinear bottom friction effect associated with the quadratic parameterization and (c) the shallow water effect arising from the nonlinear terms related to the total water depth $D = \zeta + h$ in both the continuity and momentum equations (Tang et al., 1996; Bernier and Thompson, 2007; Zhang et al., 2010; Rego and Li, 2010; Zhang et al., 2017). However, it is difficult to separate them and quantify their contributions to the interaction from the observation data. Therefore, numerical models have been extensively used to examine the mechanisms of tide-surge interaction. Wolf (1978) showed that the tide-surge interaction was dominated by quadratic friction, followed by the shallow water effect and advection process. Subsequently, Wolf (1981) further demonstrated that the shallow water effect became important for small tidal range and depth less than 10m. Using a two-dimensional numerical model of the shallow-water equations, Tang et al. (1996) demonstrated that with the tides included in the storm surge model the sea level elevation on the North Queensland coast was generally lower than that obtained by simply adding the astronomical tides to the surge, due to the quadratic bottom friction law. Rego and Li (2010) suggested that the nonlinear advection dominated in a realistic simulation, while the quadratic friction was the largest in an idealised simulation. Zhang et al. (2010) studied the tide-surge interaction in the Taiwan Strait and indicated that the nonlinear bottom

friction was a major factor to predict the elevation while the nonlinear advective terms and the shallow water effect had little contribution. 67

68

69

70

71

72

77

78

79

80

85

86 87

88

89

97

99

100

101 102

103

104

105 106

107

To quantify the contributions from each of the above three processes to the tide-surge interaction, a "subtraction" approach is widely adopted in the previous studies (Tang et al., 1996; Zhang et al., 2010; Bernier and Thompson, 2007; Zhang et al., 2017). Based on a standard model that includes all three processes, this approach assesses the changes to the interaction intensity by using a reduced model in which the nonlinear terms associated with one of the three physical processes are eliminated or linearized 73 in turn and are then subtracted from the standard model. To facilitate the quantification, various indicators have been used to represent the intensity of tide-surge interaction in different studies, e.g. the maximum 75 positive, minimum negative or root-mean-square of the tide-surge interaction induced residual elevation. 76 However, such a method is found to be defective due to the so called "rebalance" effect (Zhang et al., 2017), which means the "subtraction" approach cannot clearly separate the contributions of those three processes and quantify their relative significance to the interaction. A new approach is therefore needed to properly reveal the individual contribution to the tide-surge interaction without much interference from other processes. This is fulfilled by adopting a new "addition" approach in the present study, by quantifying 81 the interaction intensity obtained from a reduced model in which only one nonlinear process is included and comparing this intensity with that obtained from the standard model (see more details in section 5). 82 Furthermore, a new indicator of the interaction intensity is also proposed in this study, which is thought 83 to be more appropriate to quantity the relative importance of different physical processes in studying the 84 mechanism of tide-surge interaction.

The Pearl River Estuary (PRE), connecting with the Pearl River at its northern end, is the largest estuary in the Pearl River Delta (PRD). Its shape looks like an inverted funnel, with a narrow neck in the north and wide mouth opening to the South China Sea. The topography of the PRE is constituted of deep channels, shallow shoals and tidal flats, which makes the PRE extremely vulnerable to storm surges resulting from 90 typhoons or strong tropical cyclones. Based on the data from the tropical cyclone annual publication of Hong Kong Observatory (HKO, 2017), fourteen typhoons inducing high storm surges over 1 m were 92 recorded in Hong Kong (located in the south of PRE) from 1999 to 2018, two of which caused storm surge 93 elevations over 2 m. As one of these two events, the Typhoon Hato generated a pronounced storm surge along the coast of the PRE. The maximum storm surge reached 1.62 m at A-Ma station in Macau, a record 95 high in Macao since records began in 1925 (Li et al., 2018), and reached 2.79 m, 2.42 m at Zhuhai and Tsim 96 Bei Tsui of Hong Kong, respectively. Observations on the water levels and wave characteristics during the passage of Hato provided an unique dataset to assess the tide-surge interactions and the relative contributions from the three different processes. 98

The main objectives of this study are therefore to apply a three-dimensional hydrodynamic model to identify the characteristics of tide-surge interaction in the PRE during Typhoon Hato and to quantify the relative importance of the three nonlinear effects on the tide-surge interaction. In section 2, the numerical model and model configurations used in this study are briefly described. The reconstructed wind field, model simulated astronomical tides and total water levels are evaluated and validated in detail by comparing with observations in section 3. The characteristics of tide-surge interaction and its impact in the PRE for Typhoon Hato are studied in section 4. In section 5, the relative importance of three nonlinear effects on the tide-surge interaction are quantified by using the newly proposed "addition" approach. Finally, the results are summarized and concluded in section 6.

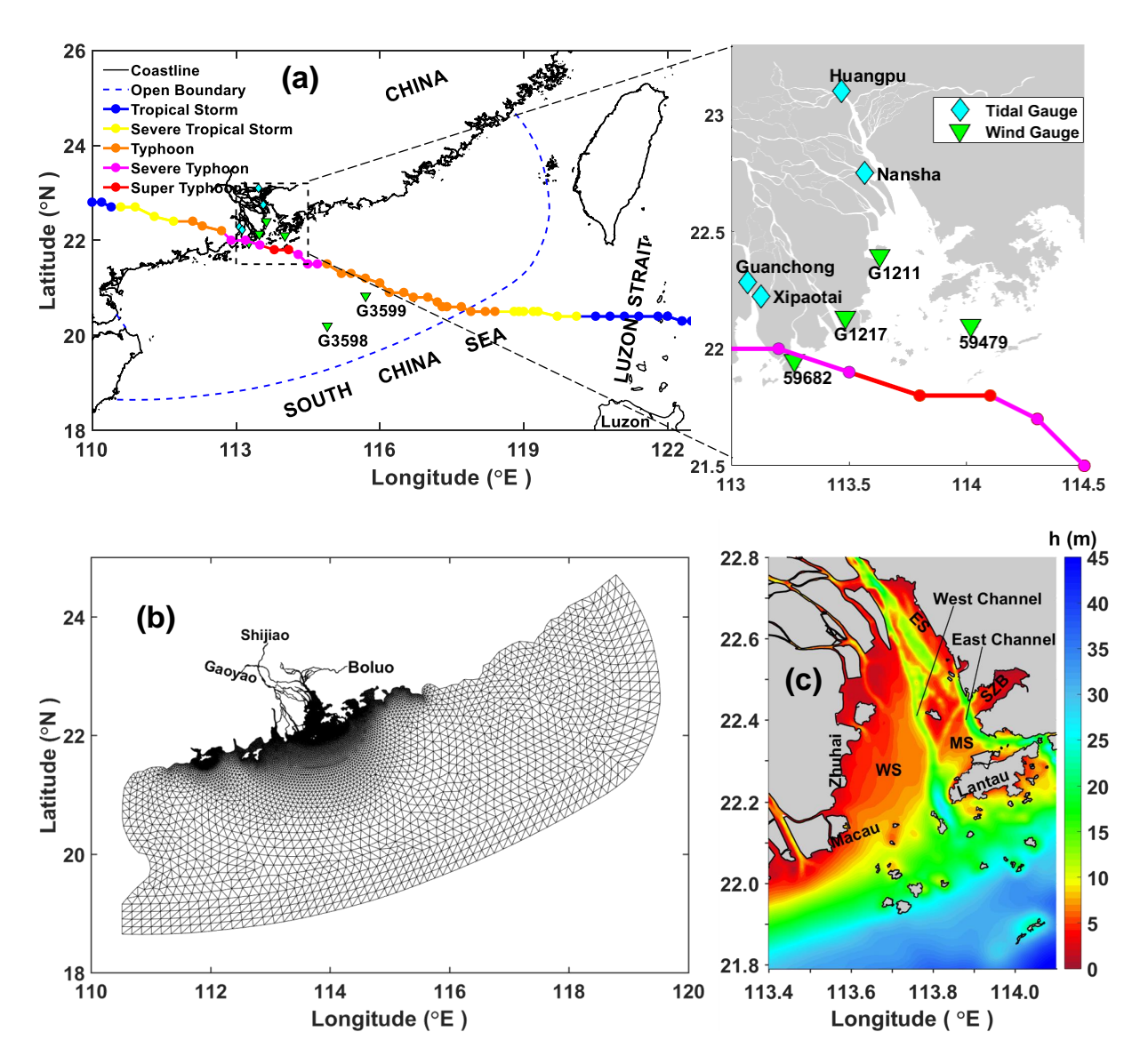


Figure 1. (a) The track and intensity of Typhoon Hato that passed the Pearl River Estuary. The model domain is bordered by blue dash lines. The eightSix downward-pointing triangles indicate the locations of wind gauges; sixfour diamonds represent the locations of tidal gauges. The information of typhoon track is provided by Zhejiang Water Resources Department (typhoon.zjwater.gov.cn), and the typhoon intensity is provided by HongKong observatory (HKO, 2017). (b) The unstructured model grid, which includes 97602 triangular elements and 56993 nodes in total; the names of three hydrological stations located at the model's river boundaries are also indicated. (c) Zoomed bathymetry around the PRE and its adjacent shelf waters. The abbreviations: WS, MS, ES and SZB mean the West Shoal, Middle Shoal, East Shoal and Shenzhen Bay, respectively.

METHODS 2

108

110

111

The Numerical Model 2.1

In this study, a prognostic, three-dimensional coastal-ocean model is applied to study the tide-surge 109 interaction in the PRE (Zheng et al., 2017b). The model is based on the Finite-Volume Community Ocean Model (FVCOM, by Chen et al. (2003)), it uses non-overlapped triangular grids in the horizontal (x and y) to resolve the complex shoreline and geometry, and the generalized terrain-following Sigma coordinate 112

113 (s) in the vertical direction to accommodate the irregular bathymetry. The mode-split approach is used 114 for the solution of circulation model, in which currents are divided into external and internal modes and 115 computed using an external and internal time step respectively (Chen et al., 2003). After the Boussinesq 116 and hydrostatic approximations, the 3D momentum and continuity equations used in FVCOM are presented 117 as follows:

$$\frac{\partial uD}{\partial t} + \frac{\partial u^2D}{\partial x} + \frac{\partial uvD}{\partial y} + \frac{\partial u\omega}{\partial s} - fvD$$

$$= -gD\frac{\partial (\zeta - \zeta_a)}{\partial x} - \frac{gD}{\rho_0} \left[\frac{\partial}{\partial x} \left(D \int_s^0 \rho ds' \right) + s\rho \frac{\partial D}{\partial x} \right] + DF_x + \frac{\partial}{\partial s} \left(\frac{K_m}{D} \frac{\partial u}{\partial s} + \frac{\nu}{D} \frac{\partial u}{\partial s} \right) \tag{1}$$

119

120
$$\frac{\partial vD}{\partial t} + \frac{\partial uvD}{\partial x} + \frac{\partial v^2D}{\partial y} + \frac{\partial v\omega}{\partial s} + fuD$$

$$= -gD\frac{\partial (\zeta - \zeta_a)}{\partial y} - \frac{gD}{\rho_0} \left[\frac{\partial}{\partial y} \left(D \int_s^0 \rho ds' \right) + s\rho \frac{\partial D}{\partial y} \right] + DF_y + \frac{\partial}{\partial s} \left(\frac{K_m}{D} \frac{\partial v}{\partial s} + \frac{\nu}{D} \frac{\partial v}{\partial s} \right) \tag{2}$$

122
$$\frac{\partial \zeta}{\partial t} + \frac{\partial uD}{\partial x} + \frac{\partial vD}{\partial y} + \frac{\partial \omega}{\partial s} = 0$$
 (3)

123 where u, v, ω are the velocity components in x, y and s directions, respectively; the vertical s coordinate

ranges from s=-1 at the bottom to s=0 at the free surface; $D=\zeta+h$ is the total water depth, ζ

125 is the surface elevation and h is the resting water depth; ζ_a is the sea level displacement induced by the

126 "inverse barometer effect"; g is the gravitational acceleration and f is the Coriolis parameter; ρ_0 and ρ are

127 the reference water density and water density, respectively; K_m and ν are the vertical eddy and molecular

128 viscosity coefficients, respectively; (F_x, F_y) represent the horizontal momentum mixing terms in the x, y

129 directions, respectively.

In the above momentum equations (i.e. Eqs. (1) and (2)), the second, third and fourth terms on the left-hand side are the advection terms (ADV); while the second term on the right-hand side represents the baroclinic pressure gradient force (which is neglected in this study). The surface and bottom boundary conditions for u, v, ω are given as follows:

$$\frac{\rho_0 K_m}{D} \left(\frac{\partial u}{\partial s}, \frac{\partial v}{\partial s} \right) = (\tau_{sx}, \tau_{sy}), \ \omega = 0 \ at \ s = 0$$
 (4)

$$\frac{\rho_0 K_m}{D} \left(\frac{\partial u}{\partial s}, \frac{\partial v}{\partial s} \right) = \left(\tau_{bx}, \tau_{by} \right), \ \omega = 0 \ at \ s = -1$$
 (5)

in which (τ_{sx}, τ_{sy}) and (τ_{bx}, τ_{by}) are the x and y components of surface wind and bottom stresses, respectively.

The quadratic law is applied in the parameterization of both the surface wind and bottom stresses as follows:

$$(\tau_{sx}, \tau_{sy}) = \rho_a C_{ds} \sqrt{U_w^2 + V_w^2} (U_w, V_w)$$
(6)

$$(\tau_{bx}, \tau_{by}) = \rho_0 C_{db} \sqrt{u^2 + v^2} (u, v)$$
 (7)

where ρ_a is the air density; C_{ds} and C_{db} are the surface wind stress and bottom drag coefficients, respectively; (U_w, V_w) are the wind speed components at a height of 10 m above sea surface in the x and y directions, respectively. In FVCOM, the surface drag coefficient C_{ds} is determined with a bulk formula as follows (Large and Pond, 1981):

$$C_{ds} \times 10^{3} = \begin{cases} 1.2 & , |\mathbf{V}_{\mathbf{w}}| < 11.0 \ ms^{-1} \\ 0.49 + 0.065 |\mathbf{V}_{\mathbf{w}}| & , 11.0 <= |\mathbf{V}_{\mathbf{w}}| < 25.0 \ ms^{-1} \\ 2.115 & , |\mathbf{V}_{\mathbf{w}}| >= 25.0 \ ms^{-1} \end{cases}$$
(8)

in which $|\mathbf{V_w}| = \sqrt{U_w^2 + V_w^2}$ is the magnitude of wind velocity; the bottom drag coefficient C_{db} is determined by matching a logarithmic bottom layer to the model at a height of z_r above the bottom, i.e.

$$C_{db} = max \left\{ \frac{\kappa^2}{\left[ln \left(\frac{z_r}{z_0} \right) \right]^2}, \ 0.0025 \right\}$$
 (9)

where $\kappa=0.4$ is the von Karman constant, z_0 is the bottom roughness parameter, and z_r is a reference height above the bed, normally equivalent to half of the height of the first grid cell above the bed (e.g. $\frac{z_r=D/[2(N-1)]}{z_r}$ and $\frac{N}{z_r}$ is the number of vertical sigma layers). It is noted that the C_{db} calculated as above is dependant on the total water depth ($D=\zeta+h$) which should also represent the nonlinear shallow water effect. This effect is eliminated by applying a constant C_{db} of 0.0025 in this study in order to cleanly separate the contribution of nonlinear bottom friction and the shallow water effect, and also for its negligible role in affecting the tide-surge interactions (Zhang et al., 2010).

151 2.2 Model Configuration in the PRE

The model domain covers the whole Pearl River Delta together with part of the South China Sea shelf. The open boundary (OB) is parallel to the coast and is placed far enough to eliminate any boundary effects to the simulation inside PRE (Figure 1). The resolution of horizontal grid is $\sim 50-200~m$ within the Pearl River network, $\sim 300-500~m$ inside the PRE and decreases from the coastline ($\sim 500-1000m$) towards offshore. The maximum grid size at OB is approximately 15 km. The resultant horizontal mesh contains a total of 97602 elements and 56993 nodes (Figure 1b). In the vertical direction 25 sigma layers are used, with uniform layer thickness of about 0.2 m inside the majority part of PRE.

The model is mainly driven by tidal forcing from open boundary and atmospheric forcing (i.e. wind stress 159 and sea level pressure) at the sea surface. Eight tidal constituents (i.e. M_2 , S_2 , N_2 , K_2 , K_1 , O_1 , P_1 , Q_1) 160 from the TPXO database (Egbert and Erofeeva, 2002) are used to generate tidal water level time series to 161 drive the model at the open boundary. The atmospheric forcing consists of hourly 10 m wind speed and sea 162 level atmospheric pressure (SLP) with horizontal resolution of 0.2°, and are obtained from the National 163 Centers for Environmental Prediction (NCEP) Climate Forecast System Reanalysis (CFSR) dataset. In 164 order to better describe the typhoon-associated wind field and SLP, a blended atmospheric forcing is used in this study by inserting an idealized wind field and SLP of a tropical cyclone, which is calculated by the 166 Holland parametric tropical cyclone model (Holland, 1980), into the original large-scale CFSR atmospheric 167

- data (see details in Section 7). In addition, high temporal resolution of hourly observed river discharge from
- three upstream hydrological stations (i.e. Gaoyao, Shijiao and Boluo) are used to represent the freshwater
- 170 inputs from the West River, the North River and the East River, respectively.
- Three sets of numerical experiments are conducted to assess the model performance and to analyse the mechanism of tide-surge interaction:
- 173 (a) Full run (Run-Full): The model is driven by both the tidal forcing at the OB and also the blended 174 atmospheric forcing. The resultant water level from this experiment model run is the storm tide (ζ_{ST}).
- 175 (b) Storm-only run (Run-SO): Only the blended atmospheric forcing is used to drive the model while the
- 176 tidal forcing is turned off. The resultant water level from this experiment model run is called pure storm surge
- 177 (ζ_{SO}) .
- 178 (c) Tide-only run (Run-TO): Only the tidal forcing is included. The resultant water level is the pure
- 179 astronomical tide level (ζ_{TO}).
- All of the above experiments are firstly spun up from resting status (i.e. zero velocity and undisturbed
- water level) for the first 4 days (from July 28 of 2017), and then the simulations are conducted continuously
- through the whole August of 2017. The split-mode time stepping method is used in this model, with a 6 s
- 183 internal time step and 1 s external time step.

3 MODEL EVALUATION AND VALIDATION

184 3.1 Wind Speed Evaluation

- As shown in Figure 1, Hato formed as a tropical depression over the sea northeast of the Luzon Island on
- 186 19 August 2017 and intensified to a tropical storm over the same waters on 20 August. It moved westwards
- across the Luzon Strait, and intensified to typhoon over the northeastern part of the South China Sea on 22
- 188 August. After that, Hato transferred west-northwest towards the coast of China where it intensified further
- and became a super typhoon at early morning of 23 August over the sea south of Hong Kong, reaching its
- 190 peak intensity with an estimated sustained wind speed of 185 km/h near its centre. After making landfall
- 191 at Zhuhai with severe typhoon intensity, Hato gradually degenerated into a low pressure on 24 August.
- Based on the above information, a reconstructed blended wind field for Typhoon Hato is created by using
- 193 the Holland parametric model (see details in Section 7). Comparing with the original CFSR wind, the
- the frontand parametric model (see details in Section 7). Comparing with the original of six wind, the
- 194 blended wind field shows a much larger wind speed near the typhoon center, and a more asymmetric vortex
- 195 structure, which has larger wind magnitude at the right side of typhoon track due to the typhoon translation
- 196 motion (Figure 2). Especially at 03:00 GMT on 23 August when Hato intensified as a super typhoon, the
- 197 blended data (Figure 2h) clearly reproduced the much stronger typhoon intensity, by contrast no obvious
- 198 vortex structure of typhoon was found in the original CFSR data (Figure 2d). Moreover, the locations of
- 199 typhoon center in the blended data are consistent with, while those in the CFSR data deviate more or less
- 200 from (e.g. Figure 2a and 2b), those taken from the best track data.
- In order to have a qualitative evaluation on both the CFSR and the blended wind speed, the observed
- 202 wind speeds from six representative wind gauge stations are collected and used in this study, including
- 203 59682 and G3599 that locate near Hato's track center and G3598 which is relatively far away, and another
- 204 two locations (i.e. G1217 and 59479) that are located near the entrance of PRE but also not far from the
- 205 tropical cyclone track and an extra one (i.e. G1211) that is located inside the PRE.

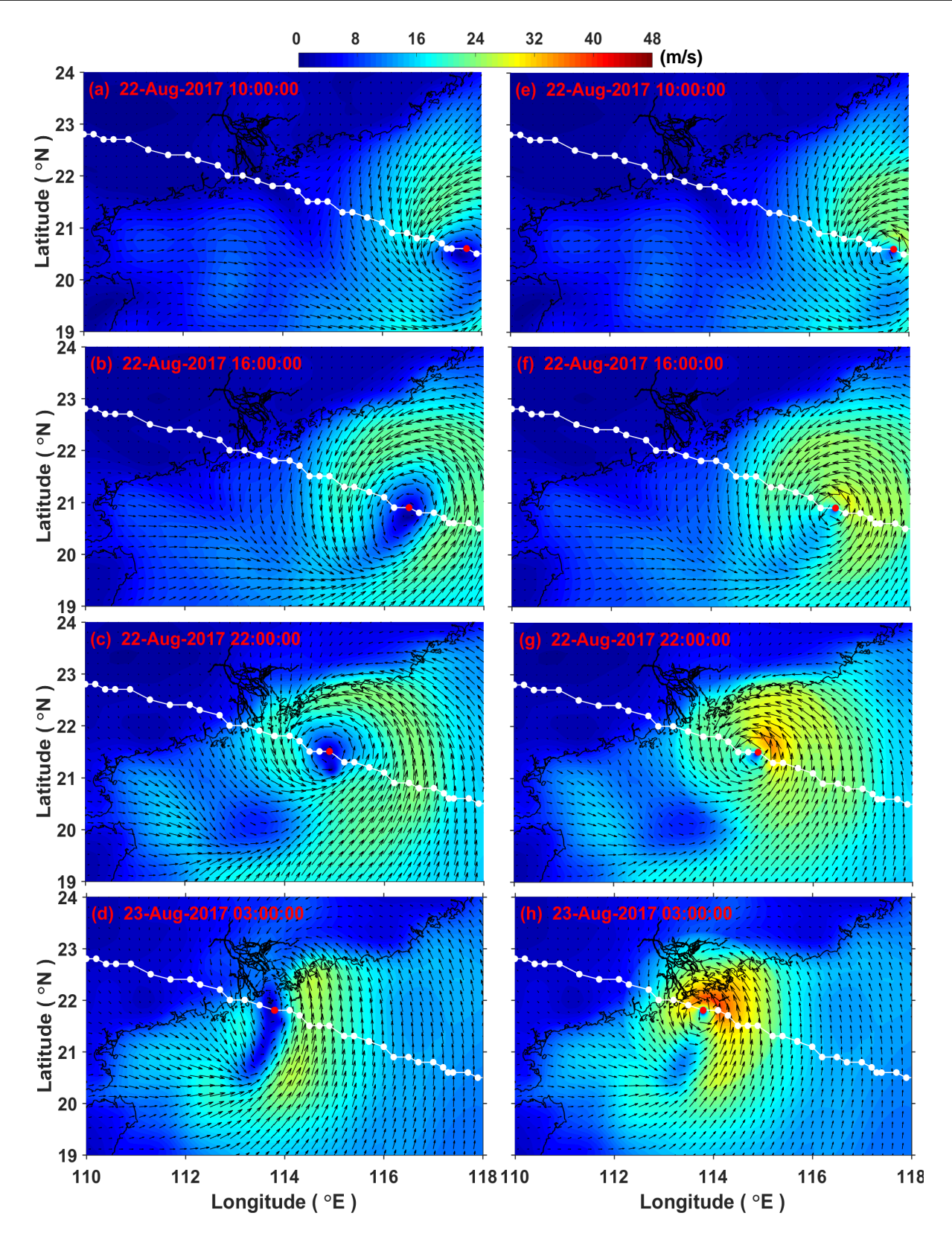


Figure 2. Wind fields from the CFSR dataset (a-d), CFSR and Holland model blended data (e-h), from 10 GMT of 22 August to 03 GMT of 23 August, 2017 when Typhoon Hato transferred over the northeastern part of the South China Sea. The white (red) solid circles represent the non-current (current) position of the hourly typhoon center provided by Zhejiang Water Resources Department (typhoon.zjwater.gov.cn)

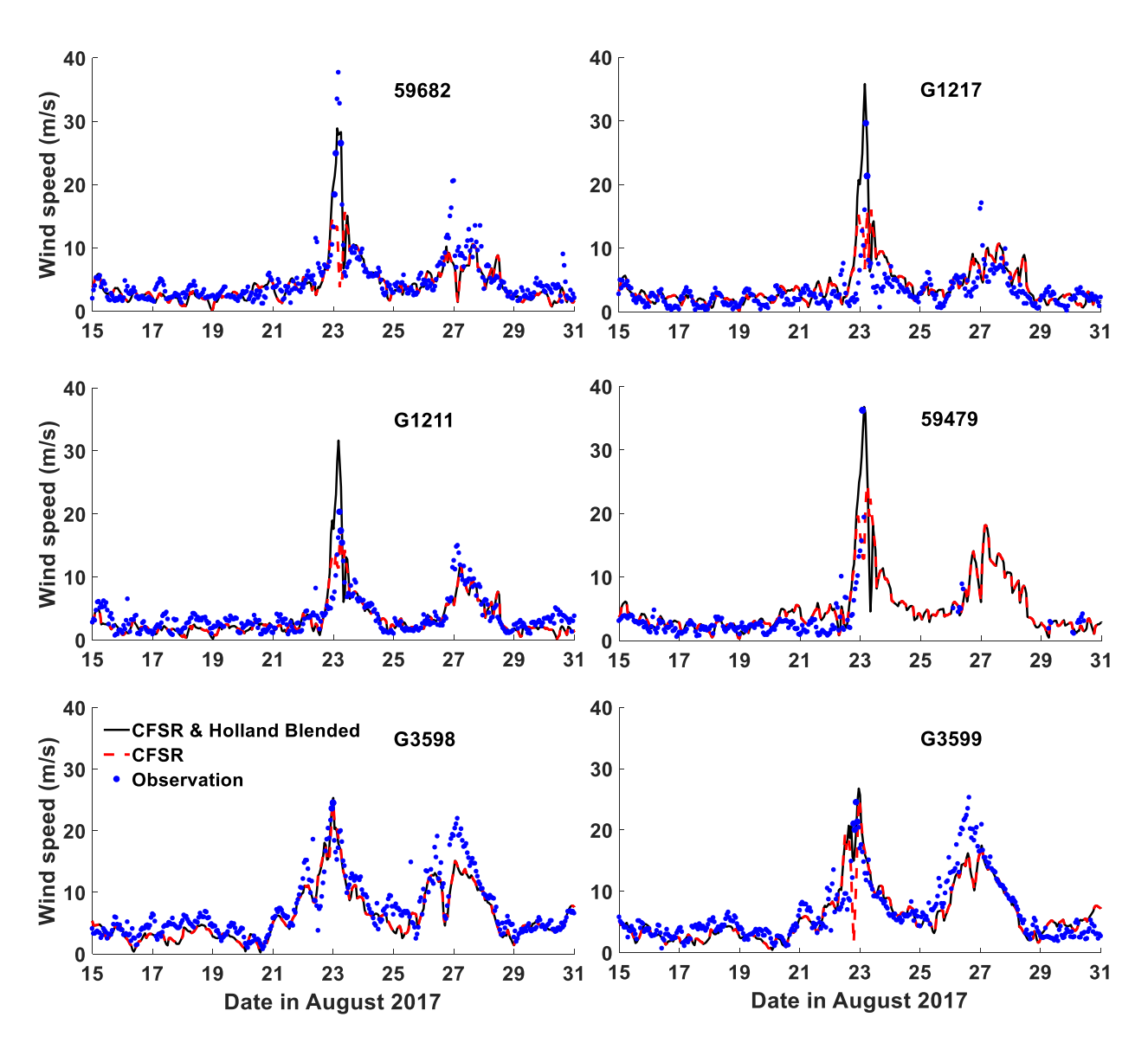


Figure 3. Comparisons of wind speed from CFSR and Holland model blended data (black line), CFSR dataset (red line), and observations (blue dots).

The observed and reconstructed wind speed at the above six stations are compared in Figure 3, in which a common feature of two notable peaks is observed in the last ten days of August. The first peak on 23 August resultes from the Typhoon Hato, while the other one is due to another typhoon Pakhar. In this research, only Hato is analysed in detail and thus the blended wind field is only created during its passage (i.e. 21-24 of August); while for the rest of time the blended wind field is identical to the CFSR dataset. Comparing with the observations, the magnitude of wind speeds based on CFSR are very close to the measurements when Hato's effects are minimal, e.g. between 15th and 21st of August when the typhoon is absent at all stations, and throughout the whole period at G3598 which is far away from the typhoon center. However, the CFSR data severely underestimates the wind speed during the passage of both Typhoon Hato and Pakhar. In contrast, the blended approach reproduces both Typhoon Hato's peak wind magnitude and timing well on the whole, although some discrepancies are still observed (e.g. G1211) due to the fact that the parametric tropical cyclone models don't account for the structural changes and wind reductions caused by the local land topographies. These comparison results suggest that a blended approach is able to achieve

220

221

222

223

reasonable well estimation of the peak wind stresses under a typhoon condition, while the CFSR data can be reasonably used with minimal typhoon impacts.

3.2 Water Level Validation

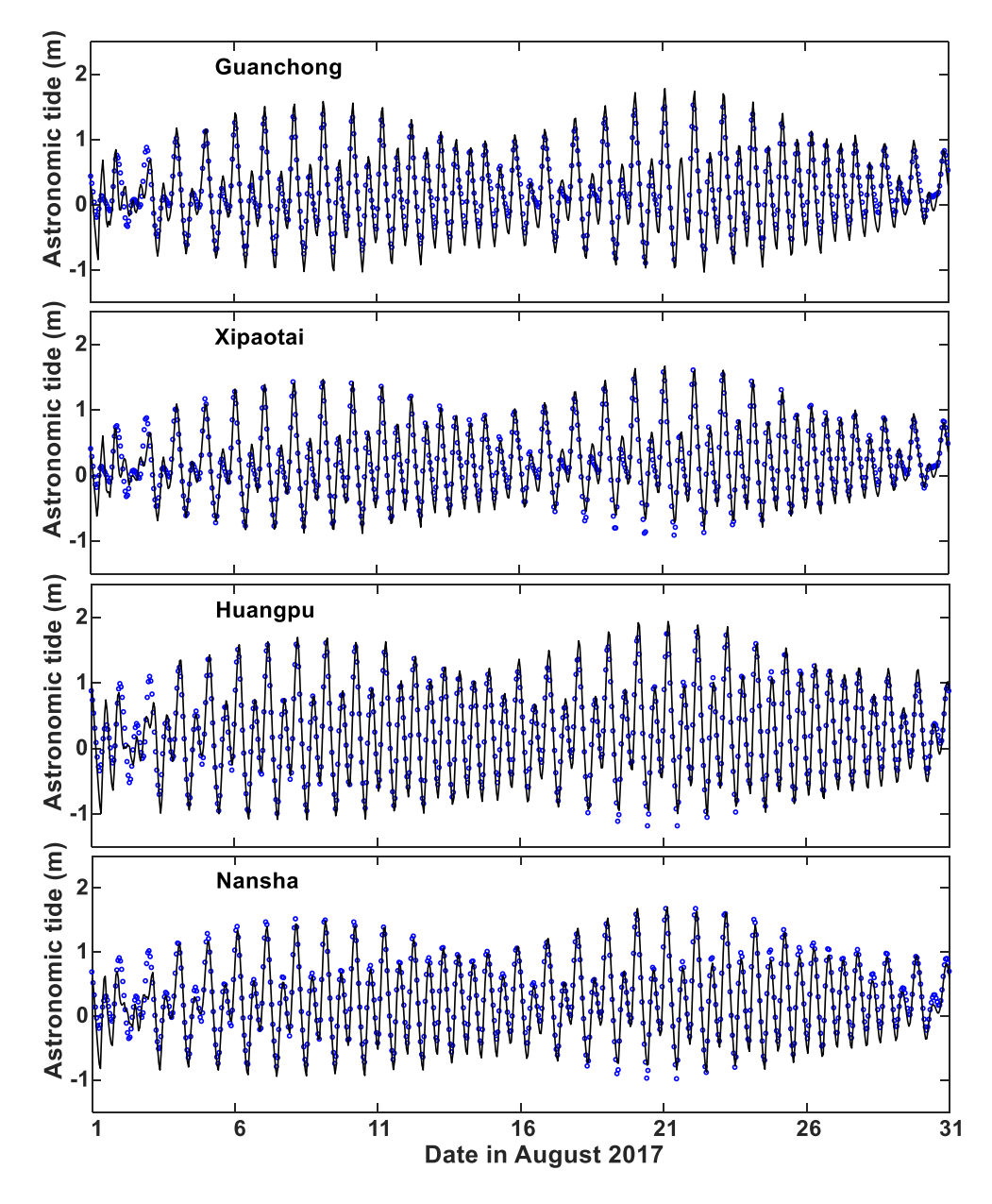


Figure 4. Comparisons of model predicted (lines) with the reconstructed (circles) astronomical tide over August 2017 at the station of Guanchong, Xipaotai, Huangpu and Nansha. The reconstructed astronomical tide are calculated from the tidal constituents that obtained from the long-term harmonic analysis of the observed total water levels.

To validate the computed water level, a root-mean-square error (RMSE), correlation coefficient (R) and model skill (Skill) are used. The RMSE indicates the average deviation of the model results from the

224 observations which is defined as

$$RMSE = \sqrt{\frac{1}{N} \sum_{n=1}^{N} (M_n - C_n)^2}$$
 (10)

where M_n and C_n are the measurements and model computed results, respectively, at N discrete points. The correlation coefficient (CCF) and model skill (Skill) evaluate the coherence between the model results and observations; a CCF or Skill value of 1 indicates a perfect agreement between the model results measurements whereas a value of 0 indicates complete disagreement. The CCF is given by

$$CCF = \frac{\frac{1}{N} \sum_{n=1}^{N} \left(M_n - \overline{M_n} \right) \left(C_n - \overline{C_n} \right)}{\sigma_C \sigma_M}$$
(11)

where σ_C and σ_M are the standard deviations of the model results and measurements, respectively; the overbar represents the mean value. Following Willmott (1981), the Skill formulation is given as follows:

$$Skill = 1 - \frac{\sum_{n=1}^{N} |M_n - C_n|^2}{\sum_{n=1}^{N} \left(|M_n - \overline{M_n}|^2 + |C_n - \overline{M_n}|^2 \right)}$$
(12)

Table 1. The evaluation of model results.

231

232

233

234

235

236

237

	Stations:	Guanchong	Xipaotai	Huangpu	Nansha
Astronomical Tide*	RMSE (m)	0.17	0.14	0.15	0.12
	CCF	0.98	0.97	0.98	0.99
	Skill	0.96	0.97	0.98	0.98
Storm Tide**	RMSE (m)	0.19 (0.28)	0.16 (0.25)	0.21 (0.34)	0.18 (0.31)
	CCF	0.96 (0.96)	0.96 (0.93)	0.96 (0.93)	0.97 (0.95)
	Skill	0.94 (0.92)	0.96 (0.92)	0.96 (0.92)	0.96 (0.93)

^{*} The M_n used to calculate *RMSE*, *CCF* and *Skill* here are the reconstructed astronomical tides from the harmonic analysis results of the observed long-term total water levels; ** calculations are conducted based on the model results using the blended atmospheric forcing, the values inside the parentheses are calculated over the period from 21 to 24 August, while those outside are calculated over the whole August of 2017.

The computed astronomical tide are evaluated first at four hydrological stations of Guanchong, Xipaotai, Huangpu and Nansha (Figure 4) over the whole simulation period (i.e. the August of 2017). As shown in Table 1, the model predictions follow the measurements very well: the RMSE values at all of four stations are less than 0.17 m, the correlation coefficient (CCF) and model skill (Skill) are generally above 0.96. The model predicted storm tide at the above four stations are further compared with the observation in Figure 5. At all of the above four stations, the observed storm tide reaches its maximum (above 2 m) on the morning of 23rd of August, shortly after Typhoon Hato makes landfall. Among these four stations,

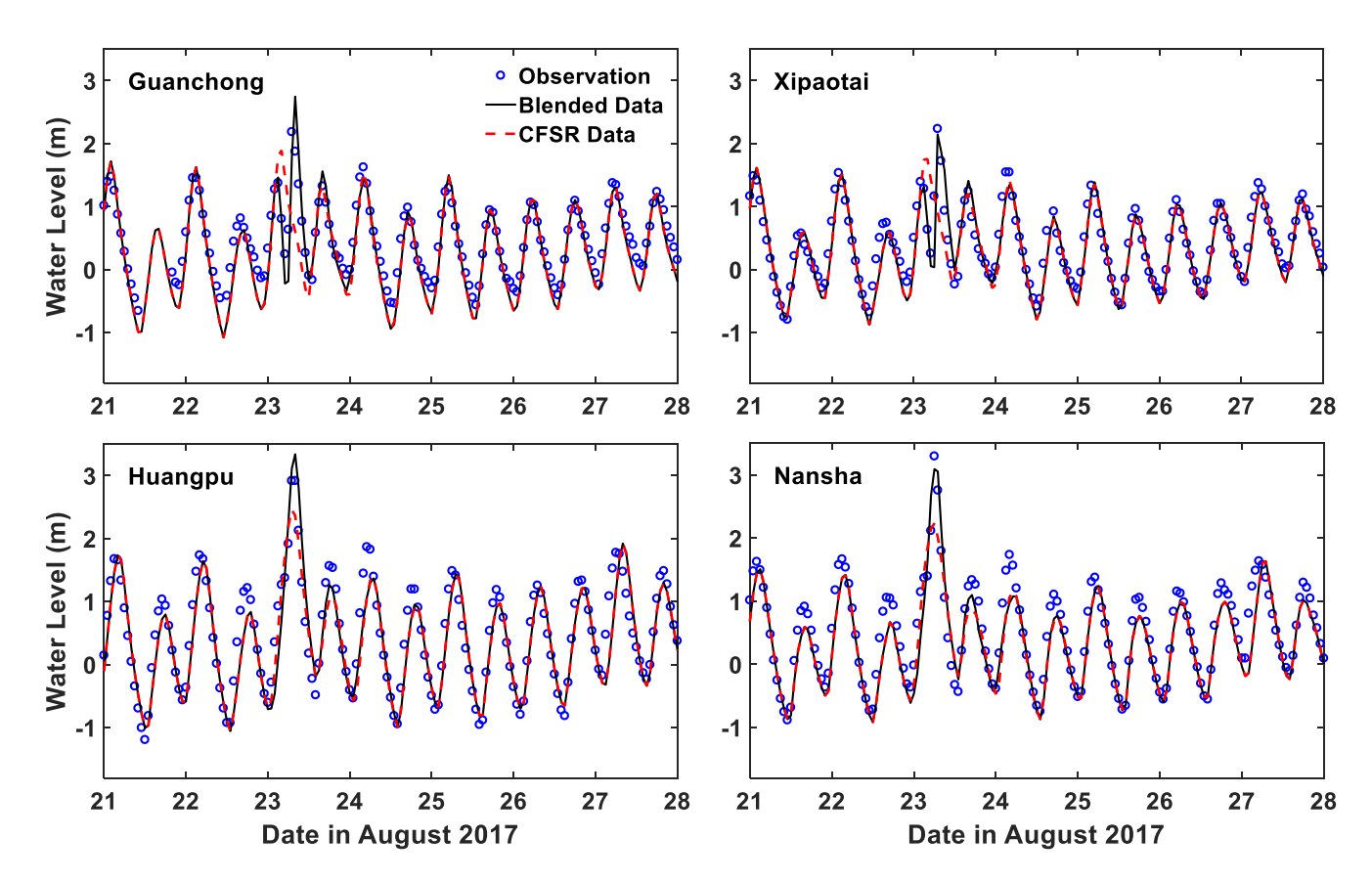


Figure 5. Comparisons of model predicted (lines) with observed (circles) time series of water level over 21-28 August 2017.

the recorded storm tide shows a pattern of a single-maximum at Huangpu and Nansha, with peak water levels of 2.92 m and 3.3 m, respectively. At the other two stations (i.e. Guanchong and Xipaotai), it is interesting to observe that the recorded water level shows a double-peak pattern of "abrupt decline and then rapid rise" in a short time period just before reaching the maximum value on the 23rd of August. This is closely related to the relevant positions of these two stations to the typhoon center, which determines the local wind direction and their relative relationship with the local geometry of the coastline. When Hato moves close but has not made landfall, these two stations are located at the right front of the typhoon center with offshore wind prevailing locally; negative storm surges are thus produced and make the local water level drop significantly. After Hato makes landing, the local wind direction transferes into onshore in a short time, with the above two stations lying at the right rear of the typhoon center. The local water level thus increases with positive storm surges produced. It is the strong local wind that leads to the significant intensity of the local drop and rise of water level; whereas the fast translation speed of Hato results in the sharp change of water levels from a local minimum to the maximum value.

When Hato is far away (i.e. before and after the 23rd of August) from the local stations, the model predicted storm tide from CFSR wind field agrees well with the observations. However, the CFSR model results severely under-estimate the maximum water levels (e.g. Nansha station) when Hato moves close, in the meantime it totally misses the "double-peak" pattern of water level observed at Guanchong and Xipaotai. By contrast, the model calculated water levels from the blended data agree well with the observations during the whole passage of Typhoon Hato, with both the storm tide maxima and the above "double-peak" pattern of water level well reproduced. The model discrepancies at the time when peak storm tides occur

are reduced from 1.37m, 1.32m, 0.46m and 1.06 m (when the original CFSR data is used) to 0.42m, 0.08m, 258 259 0.18m and 0.20m (when the blended data is used), at the station of Guanchong, Xipaotai, Huangpu and Nansha, respectively. Therefore, significant improvements on the model predicted water levels are obtained 260 261 in this study by using the blended data shown in the section 7. Table 1 also shows that the CCF (Skill) at 262 all four stations are above 0.96 (0.94), indicating an overall well agreement of the model predicted storm tide with the observations over the whole August of 2017. However, when zoom in the validation period 263 264 over 21-24 August, the CCF (Skill) reduces slightly while the RMSE increases more than 9 cm at all four 265 stations. This is largely due to the missing of some physical processes in the present model simulations, e.g. 266 wave-induced setup and non-hydrostatic pressure gradients (Zhang et al., 2017).

4 TIDE-SURGE INTERACTION AND ITS IMPACT

277

278279

280 281

282

283

284 285

Figure 6 shows the time series of the model predicted storm tide levels (ζ_{ST}), astronomical tide levels (ζ_{TO}) 267 and pure surge elevations (ζ_{SO}) at above four tidal gauges; they are water level results from the standard 268 experiment of Run-Full, Run-TO and Run-SO, respectively. In addition, two residual water elevations, i.e. 269 ζ_{PS} and ζ_{TSI} , are also included in Figure 6. The residual water elevation ζ_{PS} is calculated by subtracting 270 ζ_{TO} from ζ_{ST} , and is known as the practical storm surge as defined in most operational storm surge 271 monitoring systems (Horsburgh and Wilson, 2007; Zhang et al., 2010); while $\zeta_{TSI} = \zeta_{ST} - \zeta_{TO} - \zeta_{SO}$, is 272 the residual elevation due to the tide-surge interaction. Model results show that the magnitudes of ζ_{PS} near 273 274 the landfall of Hato are 2-3 m at four tidal gauges and are much larger than their neighbouring astronomical tidal high levels. These high water elevations overtop the coastal sea walls, bringing large amount of 275 flooding to the coastal areas of PRE (Li et al., 2018). 276

Without tide-surge interaction, the practical storm surge ζ_{PS} will be equal to the pure storm surge ζ_{SO} . However, this is generally not true as shown in Figure 6: the ζ_{PS} are not equal to ζ_{SO} during the majority of time at all four stations. The comparison of ζ_{PS} and ζ_{SO} shows a general feature that the magnitudes of ζ_{PS} are greater near the low tide waters but smaller near high tide waters than ζ_{SO} , especially in the first tidal cycle on 23rd of August when the storm surge maxima occurres. Similar results have also been reported in many previous studies, e.g. Horsburgh and Wilson (2007); Zhang et al. (2010); Rego and Li (2010); Zhang et al. (2017), reflecting the effects of tidal modulation on surge productions, which can be explained by an idealized expression on the equilibrium between sea surface slope and a constant wind stress term (Pugh, 1996) as follows:

$$\frac{\partial \zeta}{\partial x} = \frac{C_{ds} U_w^2}{qD} \tag{13}$$

Although such equilibrium is rarely established in the real world as the wind fields changes frequently, 286 the Eq. (13) indicates a fundamental point that the wind stress is more effective in producing surges in the 287 shallower waters, e.g. during the tidal low waters. In addition to the change of magnitude, the phase of 288 289 surge can also be altered by the tide-surge interaction (tidal modulation). Previous studies, e.g. Horsburgh 290 and Wilson (2007); Wolf (2009); Rego and Li (2010), have pointed out that a reduced water depth will result in reduced phase speed both directly and indirectly due to the effects of bottom friction as it is 291 inversely proportional to the water depth; whereas the enhanced water depth will increase the phase speed. 292 In consistent with the above physics, the peaks of the predicted ζ_{PS} shown in Figure 6 arrive a bit earlier 293 than that of ζ_{SO} . 294

296

297298299

300

301 302

303

304 305

306

307

308 309

310

311

312

313

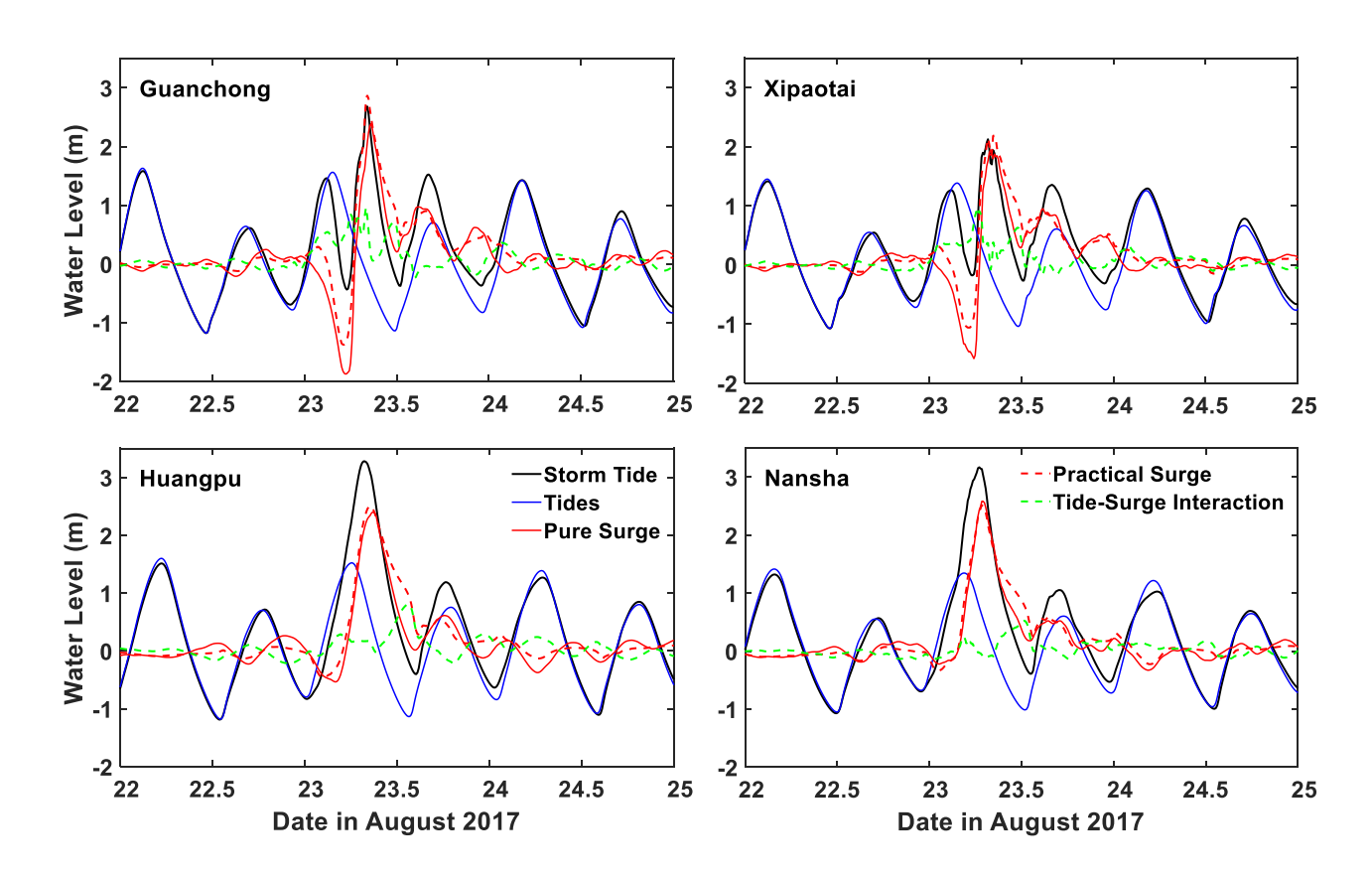


Figure 6. Time series of storm tides (ζ_{ST}) , pure astronomical tides (ζ_{TO}) , pure storm surges (ζ_{SO}) , practical storm surges (ζ_{PS}) and residual elevations due to the tide-surge interaction (ζ_{TSI}) over 22-25 August 2017 at the station of Guanchong, Xipaotai, Huangpu and Nansha.

The impact of tidal modulation (tide-surge interaction) on the storm surge and total water levels in the whole PRE can be examined in detail in Figure 7, in which the distribution of the differences between the maxima of ζ_{PS} and ζ_{SO} (i.e. $\zeta_{PS}^{max} - \zeta_{SO}^{max}$; Figure 7a), and the differences between the maximum elevations of ζ_{ST} and $\zeta_{SO} + \zeta_{TO}$ (i.e. $\zeta_{ST}^{max} - [\zeta_{SO} + \zeta_{TO}]^{max} = [\zeta_{PS} + \zeta_{TO}]^{max} - [\zeta_{SO} + \zeta_{TO}]^{max}$; Figure 7b), are presented. In these figures, two notable features can be observed: firstly, the spatial distributions of both differences defined above show considerable variations in the PRE, indicating that the effect of tide-surge interaction is highly localised and spatially varying; secondly, both the tidal modulated peak water elevations (i.e. ζ_{PS} , ζ_{ST}) have higher magnitudes near the east coast but smaller magnitudes close to the west coast of the PRE than those predicted without the effects of tide (i.e. ζ_{SO} , [$\zeta_{SO} + \zeta_{TO}$]), which confirms the previous studies (e.g. Brown et al., 2010; Quinn et al., 2012) in showing that tide-surge interaction can either enhance or reduce the peak surge elevations. More detailed examinations on the magnitudes show that the peak water elevations at the Shenzhen Bay are significantly raised by 0.1 - 0.5 m due to tide-surge interaction, whereas at the coast area of Zhuhai and Macau the peak water elevations are reduced by 0.2-0.4 m. From a surge protection point of view, the increase in the water level shown in Figure 7a and 7b are of more practically significant, as an underestimation of the peak water elevations, e.g. near the east PRE coast in this study when the effect of tide-surge interaction is not taken into account, can often lead to huge economic loss and high fatalities.

The differences in the maxima of practical storm surge ζ_{PS} and pure storm surge ζ_{SO} (i.e. $\zeta_{PS}^{max} - \zeta_{SO}^{max}$) in Figure 7a represent the tide-surge interaction induced changes in the magnitude of storm surge. By contrast,

the differences between the maximum elevations of ζ_{ST} and $\zeta_{SO} + \zeta_{TO}$ (i.e. $\zeta_{ST}^{max} - [\zeta_{SO} + \zeta_{TO}]^{max} = [\zeta_{PS} + \zeta_{TO}]^{max} - [\zeta_{SO} + \zeta_{TO}]^{max}$) in Figure 7b include the effects from the tide-surge interaction on both the magnitudes and phases of the storm surge. The fact that the tide-surge interaction not only influences the surge level but also the peak timing of the storm surge, is clearly reflected in the contrast between Figure 7a and 7b, which is also detailed in Figure 7c. A close examination on Figure 7c suggests that the phase alteration mainly increases (see those positive magnitudes) the peak total water elevations (i.e. the storm tide elevation ζ_{ST}) in the majority of PRE. One of the most notable area is near the top of Shenzhen Bay, where a maximum magnitude of 0.18 m is found which is largely caused by the phase alteration due to the nonlinear shallow water effects (see details in section 5.2). The above analysis indicates that both the tidal modulated surge production and phase alteration contribute considerably to the peak overall water elevations; a linear superposition of the atmospheric-only forced pure storm surge (ζ_{SO}) with the astronomical tide (ζ_{TO}) can deviate from the real condition significantly as shown in Figure 7 and thus the effects of nonlinear tide-surge interactions are vital important.

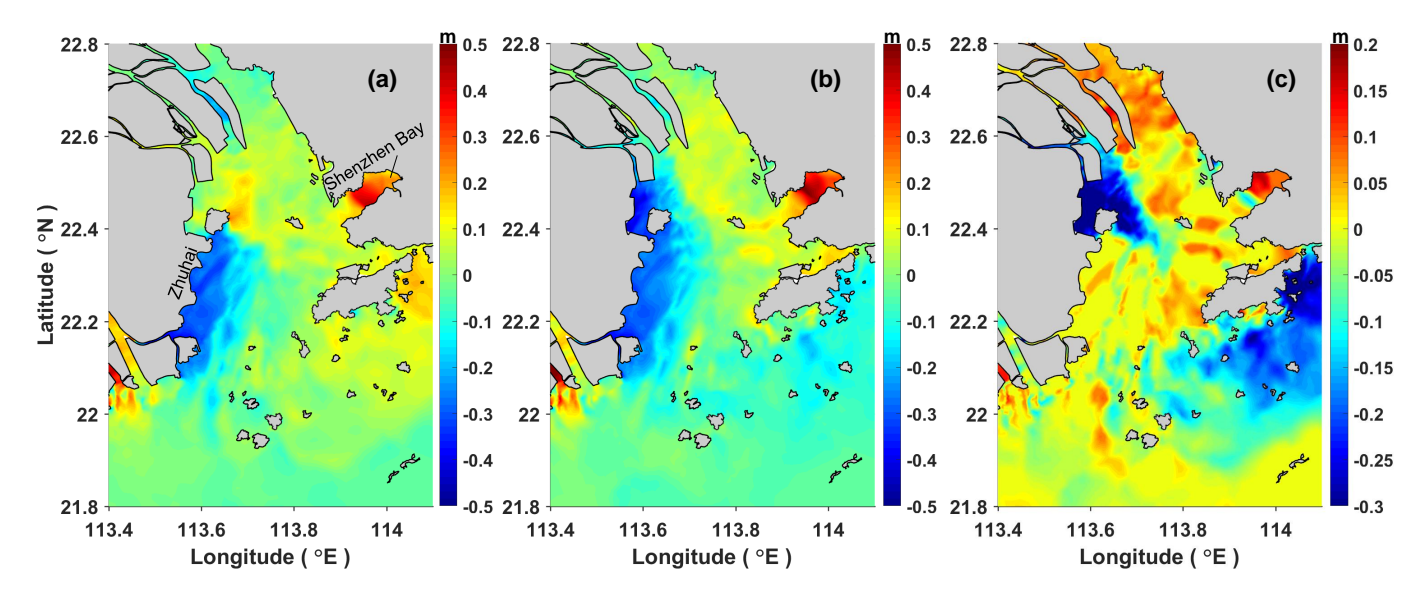


Figure 7. Spatial distributions of (a) the differences between the maximum of ζ_{PS} and ζ_{SO} (i.e. $\zeta_{PS}^{max} - \zeta_{SO}^{max}$), (b) the differences between the maximum of ζ_{ST} and $\zeta_{SO} + \zeta_{TO}$ (i.e. $\zeta_{ST}^{max} - [\zeta_{SO} + \zeta_{TO}]^{max} = [\zeta_{PS} + \zeta_{TO}]^{max} - [\zeta_{SO} + \zeta_{TO}]^{max}$), and (c) the differences between (a) and (b) $\left(i.e. \left\{\zeta_{ST}^{max} - [\zeta_{SO} + \zeta_{TO}]^{max}\right\} - \left\{\zeta_{PS}^{max} - \zeta_{SO}^{max}\right\}\right)$, during the passage of Typhoon Hato.

As noted by previous studies (Horsburgh and Wilson, 2007; Wolf, 2009; Rego and Li, 2010), the modulation of surge production and propagation shown above represents the effect of tide on the surge, while the effect of surge on the tide is largely presented as a phase shift of the tidal signal. These mutual influences between the tide and surge contribute to the total effects of tide-surge interaction. Since the residual water elevation ζ_{TSI} , calculated as $\zeta_{ST} - \zeta_{TO} - \zeta_{SO}$, is the result of tide-surge interaction, it has been taken as a direct measure of the interaction intensity in previous researches (e.g Bernier and Thompson, 2007; Zhang et al., 2010; Rego and Li, 2010; Zhang et al., 2017). Figure 6 shows that the ζ_{TSI} is negligible before and after the passage of Typhoon Hato and it increases greatly in magnitude as the storm surge develops at all stations. Notable oscillations are found in ζ_{TSI} with the near-tidal period, which is very likely due to the effect of tidal modulation. To quantify the absolute intensity of tide-surge interaction, some studies (e.g. Horsburgh and Wilson, 2007; Rego and Li, 2010; Zhang et al., 2017) use various different indicators, including the maximum positive (MAX) or minimum negative

340

341

342

343

344

345

346

347

348

349

350

351

352

353

355

356

358

(MIN) magnitude of ζ_{TSI} , whereas some others (e.g. Bernier and Thompson, 2007; Rego and Li, 2010; Zhang et al., 2010) use the root-mean-square (RMS) of ζ_{TSI}^{c0} , as the representative variable. Evidently, RMS(ζ_{TSI}) represents the average intensity of tide-surge interaction while the MAX(ζ_{TSI}) or MIN(ζ_{TSI}) concerned more on the maximum intensity that occurs during an entire typhoon event. For Typhoon Hato, the spatial distribution of MAX(ζ_{TSI}) and RMS(ζ_{TSI}) in the PRE are shown in Figure 8a and 8b, respectively. Both of these two figure demonstrate a feature that the intensity of tide-surge interaction is strongest in the top of the PRE and Shenzhen Bay and it gradually decreases from the estuary/bay head to the estuary/bay entrance, as the bell-shaped geometry can amplify the impact of tide-surge interaction. The MAX(ζ_{TSI}) is about 0.18-0.6 m in the PRE, whereas the magnitude of RMS(ζ_{TSI}) is much smaller (0.07-0.25 m). The contrast between MAX (ζ_{TSI}) and RMS (ζ_{TSI}) indicates that the effect of tide-surge interaction varies strongly over the time, which coincides with the distribution pattern of ζ_{TSI} as shown in Figure 6 that the majority energy of tide-surge interaction concentrates near the time when the largest storm surge happens. Besides the MAX(ζ_{TSI}) and RMS(ζ_{TSI}), a new indicator I_r is also plotted in Figure 8c. It is defined as the ratio of RMS(ζ_{TSI}) to square root of the product of RMS(ζ_{SO}) and RMS(ζ_{TO}), i.e. $I_r = RMS(\zeta_{TSI})/\sqrt{RMS(\zeta_{SO}) * RMS(\zeta_{TO})}$, and is used to reflect total relative intensity of tide-surge interaction to pure storm surge and pure astronomical tide, similar to that in Zhang et al. (2010). Similar feature is found in Figure 8c as that shown in Figure 8a and 8b. As the intensity of tide-surge interaction increases in proportion to both surge height and tidal range (Horsburgh and Wilson, 2007), I_r is considered to be more appropriate to quantify the relative importance of different physical processes in studying the mechanisms of tide-surge interaction (see details in section 5).

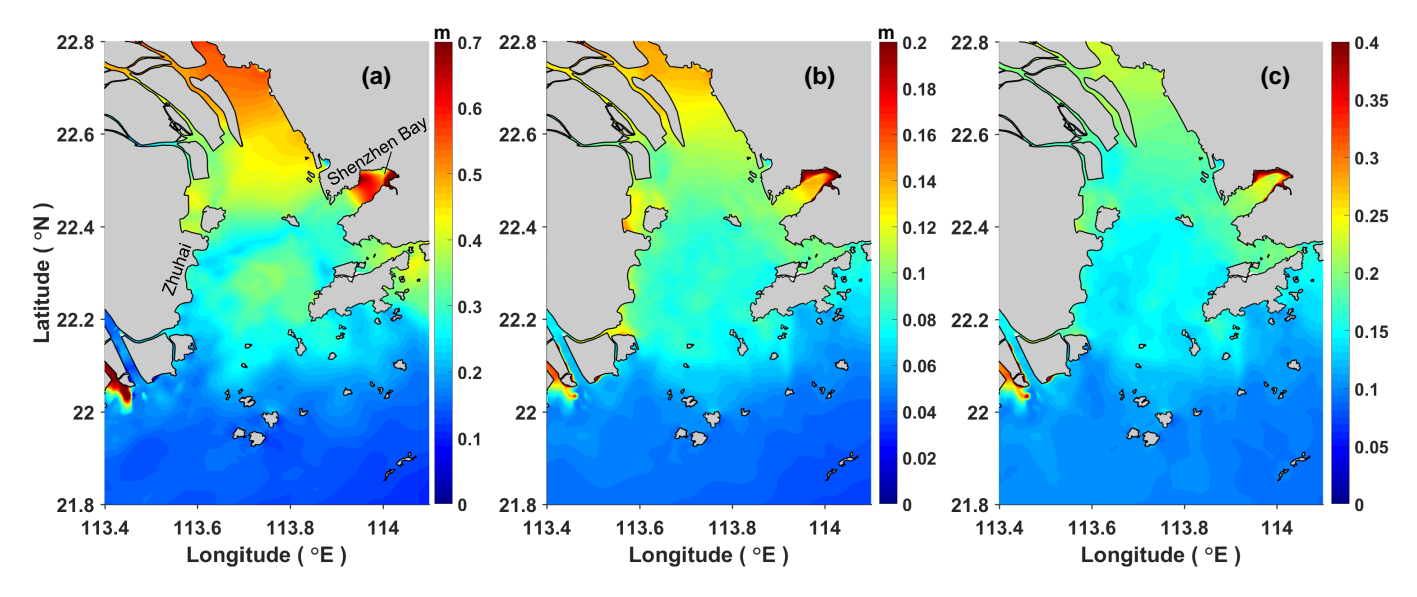


Figure 8. Spatial distributions of (a) the maximum positive magnitude of ζ_{TSI} , i.e. $\text{MAX}(\zeta_{TSI})$; (b) the root-mean-square of ζ_{TSI} , i.e. $\text{RMS}(\zeta_{TSI})$; and (c) the ratio I_r which is defined as $I_r = RMS(\zeta_{TSI})/\sqrt{RMS(\zeta_{SO})*RMS(\zeta_{TO})}$; in the PRE during the passage of Typhoon Hato.

The root-mean-square (RMS) of ζ_{TSI} is defined as $RMS(\zeta_{TSI}) = \sqrt{\int_{\Delta T} \zeta_{TSI}^2 dt/\Delta T}$; in which ΔT represents the duration of typhoon event.

5 MECHANISM ANALYSIS OF THE TIDE-SURGE INTERACTION

5.1 The "subtraction" approach

To assess the contribution of each nonlinear physical process to the tide-surge interaction, previous studies 360 (Zhang et al., 2010; Bernier and Thompson, 2007; Zhang et al., 2017) conducted numerical experiments 361 using a reduced model approach in which the nonlinear terms associated with each physical process were 362 eliminated or linearized: (1) to quantify the nonlinear advective effect (Exp-LAdy), the advective terms 363 were removed from the Eqs. (1) and (2); (2) to quantify the nonlinear bottom friction effect (Exp-LBot), the 364 quadratic form of bottom friction was linearized by using $(\tau_{bx}, \tau_{by}) = \rho_0 C_{db}(u, v)$; and (3) to quantify the 365 shallow water effect (Exp-LSW), the total water depth $D = h + \zeta$ in the governing equations was replaced 366 by h. Therefore, this approach can be regarded as a "subtraction approach" as it is based on a standard 367 model that includes all three processes and assesses the changes to the interaction intensity after one of the 368 processes is removed. Various aspects of this approach are also briefly summarized in Table 2. Following 369 the same procedure as in the standard experiment (Exp-SD, i.e. the experiment conducted by using the 370 complete model including all three processes), three model runs (i.e. Run-Full, Run-TO and Run-SO) 371 372 are conducted in each reduced-model experiment from which the corresponding residual elevations due to tide-surge interaction (i.e. ζ_{TSI}^{LAdv} , ζ_{TSI}^{LBot} and ζ_{TSI}^{LSW}) are calculated in the same way as in the standard 373 experiment (Section 4). The contribution from each process is then assessed by quantifying the extent to 374 375 which the intensity of tide-surge interaction is reduced. For this purpose, Zhang et al. (2010) calculated a reduction ratio I_p whereas Zhang et al. (2017) closely compared the MAX(ζ_{TSI}) calculated by the reduced 376 experiments with that obtained from standard experiment. The reduction ratio I_p is defined as follows 377 (Zhang et al., 2010): 378

$$I_p = \frac{RMS(\zeta_{TSI}^{SD}) - RMS(\zeta_{TSI}^*)}{RMS(\zeta_{TSI}^{SD})} \times 100\%$$
(14)

where $RMS(\zeta_{TSI}^{SD})$ and $RMS(\zeta_{TSI}^{*})$ are root-mean-square of ζ_{TSI} obtained from the standard experiment and reduced experiments, respectively; and * represents either LAdv, LBot or LSW.

Although the contribution from each process can be discerned on close comparisons of the interaction intensity between the results from a reduced model and the standard model as in Zhang et al. (2017), it is best visualised from the detailed analysis of the differences obtained by subtracting the interaction intensity of a reduced model from that of the standard model. The reduction rate R_o , based on a generalized form of the I_P in Eq.(14), is employed to quantify the reduction of tide-surge interaction intensity as follows:

$$R_o = \frac{P^{SD} - P^*}{P^{SD}} \times 100\% \tag{15}$$

386 where P is a general indicator used to represent the intensity of tide-surge interaction, e.g. $MAX(\zeta_{TSI})$, 387 $RMS(\zeta_{TSI})$ or I_r ; SD represents the standard experiment and * represents either LAdv, LBot or LSW.

The calculated R_o over the PRE are shown in Figure 9a-c, Figure 9d-f and Figure 9g-i for the reduced experiment of Exp-LAdv, Exp-LBot and Exp-LSW, respectively. All three indicators, $MAX(\zeta_{TSI})$, $RMS(\zeta_{TSI})$ and I_r , are used to represent the intensity of tide-surge interaction and to calculate the corresponding R_o . In the present approach, the contribution from each physical process is expected to lead to positive nonnegative reduction rate (R_o) , with its magnitude indicating the strength of contribution.

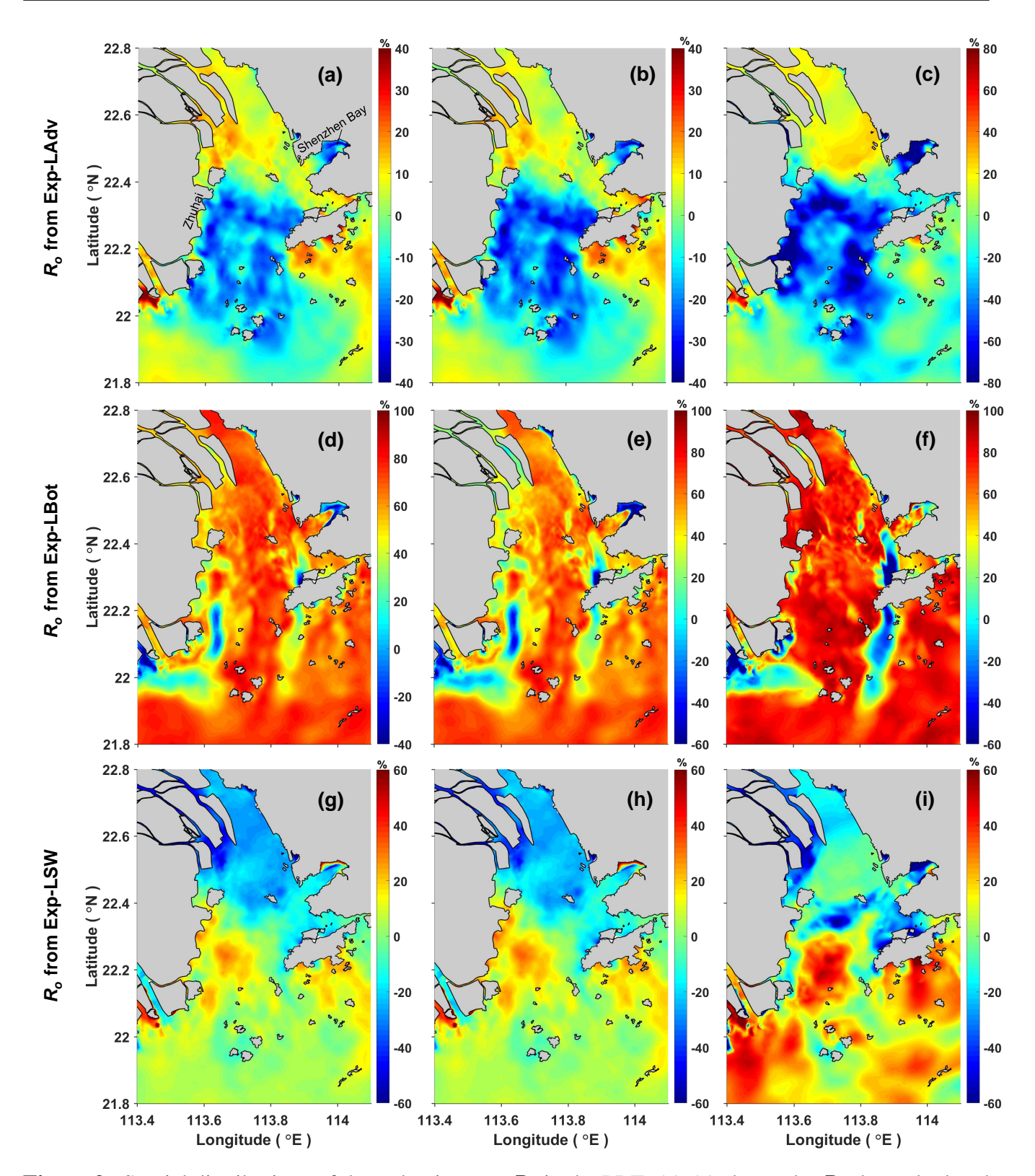


Figure 9. Spatial distributions of the reduction rate R_o in the PRE. (a)-(c) shows the R_o that calculated by using $RMS(\zeta_{TSI})$, I_r and $MAX(\zeta_{TSI})$, respectively, from the reduced experiment Exp-LAdv; (d)-(f) shows the R_o that calculated by using $RMS(\zeta_{TSI})$, I_r and $MAX(\zeta_{TSI})$, respectively, from the reduced experiment Exp-LBot; (g)-(i) shows the R_o that calculated by using $RMS(\zeta_{TSI})$, I_r and $MAX(\zeta_{TSI})$, respectively, from the reduced experiment Exp-LSW.

395

396

397

398

399 400

401

402

403

404

405

406

407

408

409

410

411

412

413

414 415

416

417

418

419

420

Name	Brief Description	Purpose	
Exp-SD Including all three nonlinear effects		Standard experiment	
Exp-LAdv	Remove advective	To assess the nonlinear advective effect	
	terms in Eqs. (1) and (2)		
Exp-LBot	Linearize bottom	To assess the nonlinear bottom friction effect	
	friction by using		
	$(\tau_{bx}, \tau_{by}) = \rho_0 C_{db} (u, v)$		
Eve I CW	Replace the total	To assess the shallow water effect	
Exp-LSW	water depth D with h		

Table 2. The "subtraction" numerical approach used to study the mechanisms of tide-surge interaction

However, negative values of R_o are found in all three reduced experiments based on all three intensity indicators (RMS, I_r and MAX) in Figure 9a-i. This common feature suggests that it is more likely that the "subtraction" approach is the reason for the negative reduction rate, rather than inappropriate indicators are used. Similar results are also observed in several previous studies (e.g. Tang et al., 1996; Zhang et al., 2017). As explained in Zhang et al. (2017), this phenomenon is due to the "rebalance" effect: in each of three reduced experiment, when one physical process is removed, the remaining other two processes will increase their strength to rebalance the govern equations, a larger intensity of tide-surge interaction induced by these two processes is thus obtained which leads to a negative R_o . Furthermore, the change of the strength of remaining two processes (say the nonlinear bottom friction effect and shallow water effect) indicates that the tide-surge interaction intensities induced by these two processes from a reduced model (i.e. P^*) are different with those included in the standard model (i.e. those included in P^{SD}). Even if the value of $P^{SD} - P^*$ is positive, it may not be the correct intensity induced by the first process (say the nonlinear advective effect). This means that, in addition to the negative R_o , the positive R_o can also be influenced by the "rebalance" effect. The R_o shown in Figure 9, no matter positive or negative, thus can not correctly represent the contribution from one nonlinear process properly. An "addition" approach is therefore developed to improve the analysis.

5.2 The "addition" approach

Due to the defects found in the above "subtraction" numerical approach, a new method is proposed in this section in order to clearly separate the contributions of three physical processes and quantify their relative contributions to the tide-surge interaction. As introduced in section 5.1, the "subtraction" approach quantifies the contribution of one specific process to the tide-surge interaction by removing/linearizing its corresponding momentum term from the standard model. After this operation, each reduced model still contains two of three nonlinear effects. In contrast, the present new approach takes an "addition" approach (Table 3): (a) firstly, a base experiment (Exp-None) is conducted using a reduced model with all three nonlinear effects removed; (b) three experiments (Exp-AAdv, Exp-ABot, Exp-ASW) are further carried out, each only takes one nonlinear effect into account; (c) following the same way as in the standard experiment and the "subtraction" approach, the surges (ζ_{SO}) and tide-surge interaction residuals (ζ_{TSI}) corresponding to the above four experiments are obtained.

429

430

431

432

433

434

435

436

437

438

439

440

441

442

443

444

445

446

447

448

449 450

Name	Brief Description	Purpose	
Exp-SD	Includes all three nonlinear effects	Standard experiment	
Exp-None	Remove all three nonlinear effects	Base experiment	
Exp-AAdv	Exp-None +	To assess the nonlinear	
	advective terms in Eqs. (1) and (2)	advective effect	
Exp-ABot	Exp-None +	To assess the nonlinear	
	quadratic bottom friction	bottom friction effect	
Exp-ASW	Exp-None +	To assess the shallow	
	$D = \zeta + h$	water effect	

Table 3. The new numerical approach used to study the mechanisms of tide-surge interaction

To assess the quantification of the contribution from each physical process to the tide-surge interaction, a new ratio R_n is defined as follows:

$$R_n = \frac{P^{**} - P^{None}}{P^{SD}} \times 100\% \tag{16}$$

where P is the general indicator used to represent the intensity of tide-surge interaction as used in Eq. (15); SD represents the standard experiment and ** represent either AAdv, ABot or ASW. It should be noted that although the ζ_{TSI} obtained from the base experiment (Exp-None) shall be nil theoretically as all three nonlinear physical processes are removed, it in fact has a magnitude of O(mm) due to the existence of numerical errors.

As only one process is included in a specific reduced model, this approach can avoid the "rebalance" process that occurrs in the "subtraction" approach the interaction intensity induced by this process will not be affected by the other two processes. Figure 10 shows the calculated R_n from the reduced experiment of Exp-AAdv (Figure 10a-c), Exp-ABot (Figure 10d-f), and Exp-ASW (Figure 10g-i), respectively, by using all of three representative intensity indicators. As expected, positive R_n values are obtained in all cases. For the same reduced experiment, the spatial distribution pattern of R_n calculated from $RMS(\zeta_{TSI})$ is very close to that from I_r , indicating these two indicators of interaction intensity, $RMS(\zeta_{TSI})$ and I_r , provide similar quantification to the relative contributions from the physical processes. However, the spatial distribution of R_n calculated from $RMS(\zeta_{TSI})$ (or I_r) and that from $MAX(\zeta_{TSI})$ are very different. This can be explained as both $RMS(\zeta_{TSI})$ and I_r represent the average intensity whereas the MAX(ζ_{TSI}) represents the maximum intensity of tide-surge interaction that occurs during an entire typhoon event. In the mean time, the magnitudes of R_n calculated from $RMS(\zeta_{TSI})$ and I_r also differ from each other, indicating that the pure storm surge levels (ζ_{SO}) and pure astronomical tide elevation (ζ_{TO}) in the reduced experiments are affected due to the tide-surge interaction in the typhoon event. As the tide-surge interaction increases in direct proportion to both surge height and tidal range, a larger $RMS(\zeta_{TSI})$ or $MAX(\zeta_{TSI})$ in the reduced experiment may directly be due to the larger surge height and/or the larger tidal range, but not has to be due to the corresponding physical processes themselves. Therefore, it is not appropriate to use $RMS(\zeta_{TSI})$ or $MAX(\zeta_{TSI})$ to represent the contributions from the three physical processes to the tide-surge interaction. In contrast, the ratio I_r , as shown in Eq. (16), reflects the total relative intensity of tide-surge interaction to the pure storm surge and pure astronomical tide, thus eliminates the influences of the change of surge height and tidal range on quantifying the interaction intensity. It is therefore more reasonable to use I_r rather than $RMS(\zeta_{TSI})$ and $MAX(\zeta_{TSI})$ to quantify the relative contribution from the three physical processes.

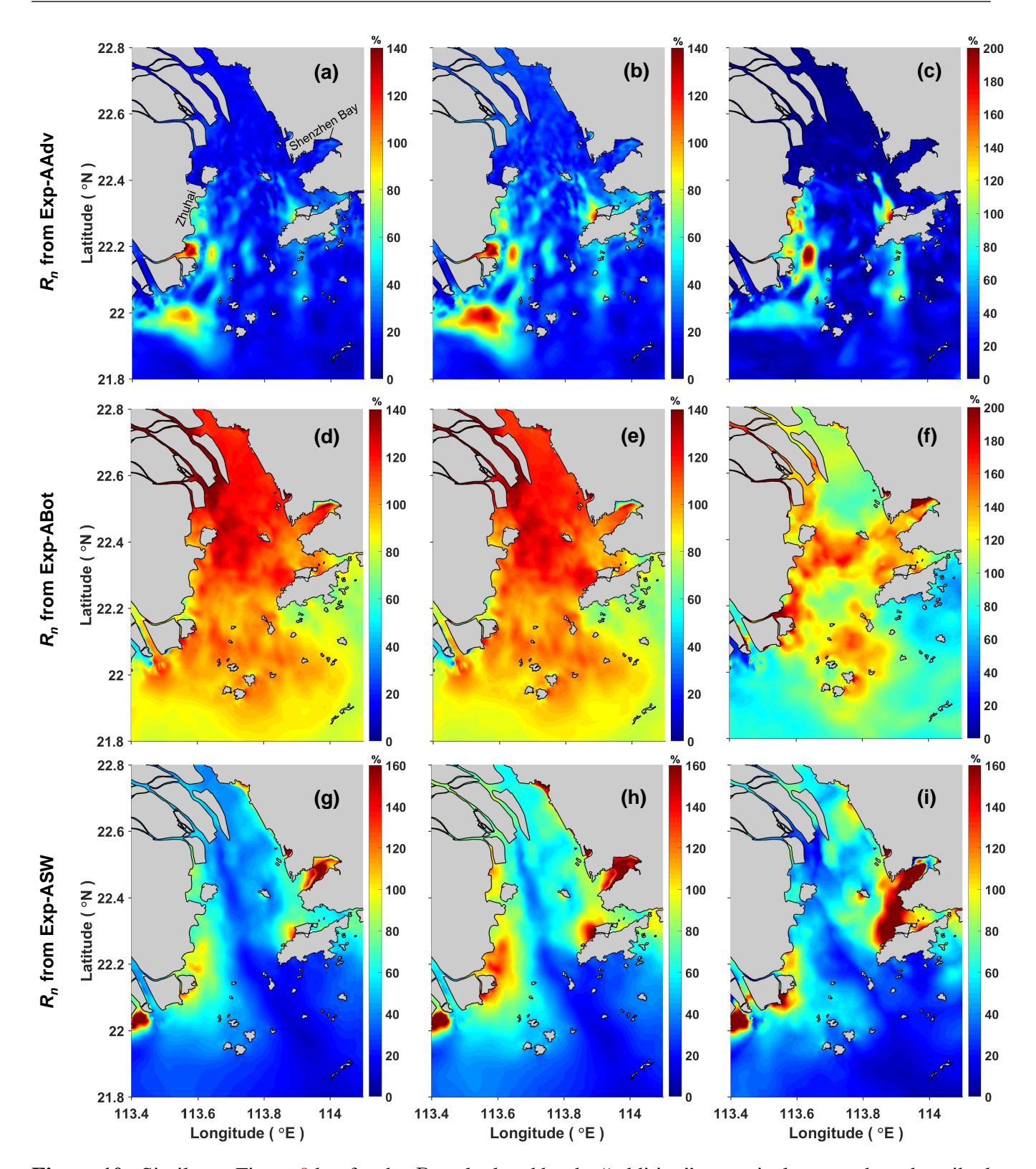


Figure 10. Similar as Figure 9 but for the R_n calculated by the "addition" numerical approach as described in section 5.2. (a)-(c) shows the R_n that calculated by using $RMS(\zeta_{TSI})$, I_r and $MAX(\zeta_{TSI})$, respectively, from the reduced experiment Exp-AAdv; (d)-(f) shows the R_n that calculated by using $RMS(\zeta_{TSI})$, I_r and $MAX(\zeta_{TSI})$, respectively, from the reduced experiment Exp-ABot; (g)-(i) shows the R_n that calculated by using $RMS(\zeta_{TSI})$, I_r and $MAX(\zeta_{TSI})$, respectively, from the reduced experiment Exp-ASW.

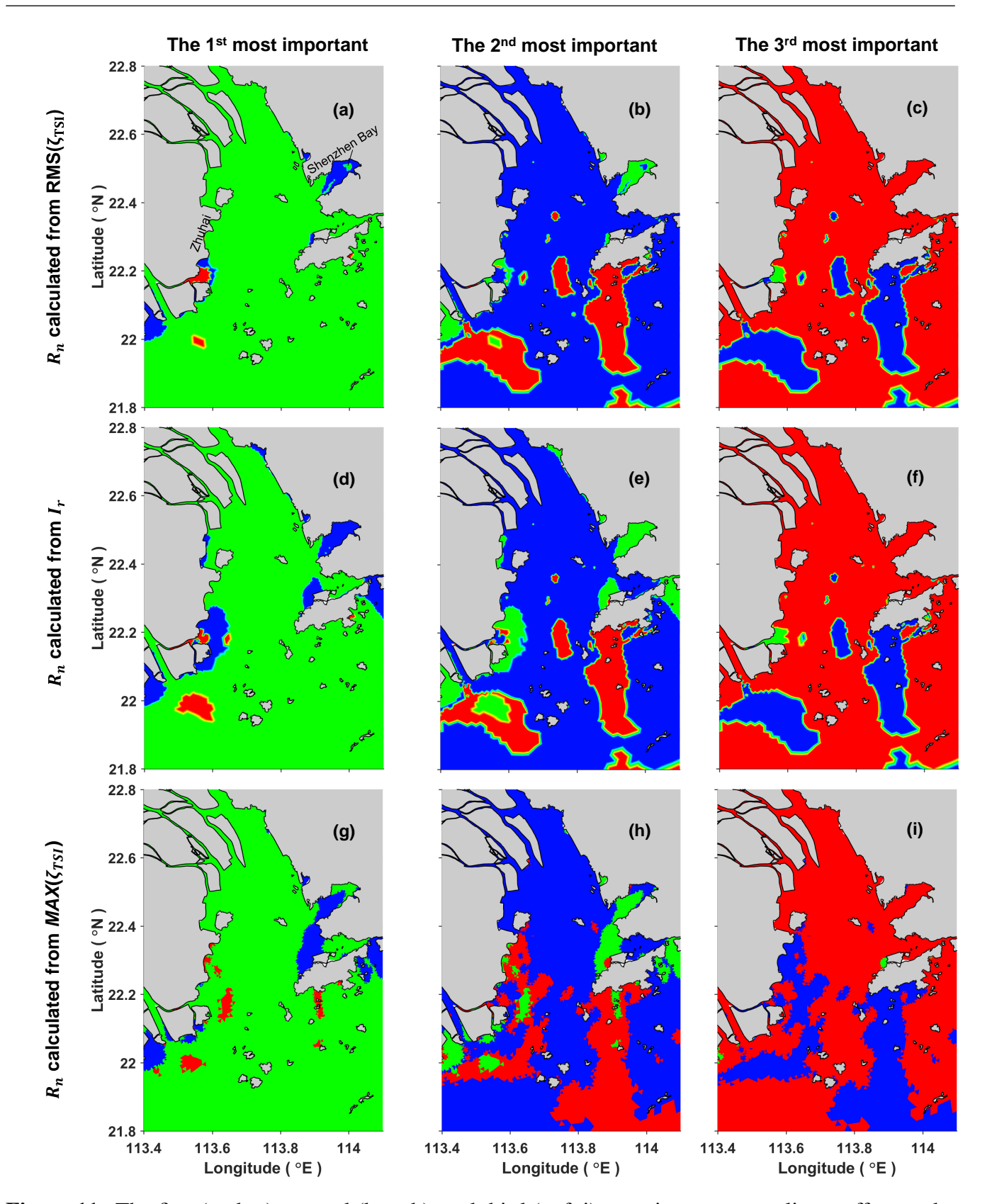


Figure 11. The first (a, d, g), second (b, e, h), and third (c, f, i) most important nonlinear effect to the tide-surge interaction in PRE. The green color represents the quadratic bottom friction; blue color represents the shallow water effect; and the red color represents the nonlinear advective effect. (a-c) use $RMS(\zeta_{TSI})$ to calculate R_n ; (d-f) use I_r to calculate R_n ; and (g-i) use $MAX(\zeta_{TSI})$ to calculate R_n .

Results in Figure 10 d-f also show a common feature that the calculated R_n in some areas of PRE is larger than 100%, indicating that the intensity of tide-surge interaction due to one of those processes alone is larger than that obtained from the standard model in which all three are included. This is a very interesting result, which suggests that certain interactions must have taken place between those three processes, and for some areas in PRE the result of this interaction is to reduce the magnitude of the contribution from individual process. In addition, this phenomenon may also be one of the reasons that the "rebalance effect" described in section 5.1 occurs: when one of the three physical processes is removed from the standard model, the remaining processes in the reduced model still interact with each other in somewhat different way; the "rebalance effect" thus occurs. It therefore further indicates that the "addition" approach is a better choice to avoid the complication in the quantification to the tide-surge interaction.

From Figure 10, the relative contribution from the three processes to the tide-surge interaction can be directly compared based on the magnitude of R_n obtained from the three reduced experiments in specific regions in the PRE. For instance, the results demonstrate that the quadratic bottom friction is most significant in the majority of the PRE, whereas in the top of Shenzhen Bay the shallow water effect is more significant due to the limited depth above the tidal flat. To get an clear overview of the overall contribution from the three processes in the whole PRE, the R_n values obtained from the three reduced models are firstly compared with each other and then sorted at every model grid according to their magnitudes. Subsequently, based on the $RMS(\zeta_{TSI})$ indicator, the process with the largest R_n value at each grid node is plotted using its specific color code in Figure 11a. Similarly, the process with the second R_n is presented in 11b and the smallest R_n in 11c. Taking the top of Shenzhen Bay as an example, Figure 11a shows the most important nonlinear process there is the shallow water effect (represent in blue color); the second most important nonlinear process shown in Figure 11b is the quadratic bottom friction (represent in green color), and the third most important nonlinear process shown in Figure 11c is the nonlinear advective effect (represent in red color). In a similar way, the process with the largest R_n , second R_n and smallest R_n based on the I_r indicator is shown in Figure 11d-f and based on the $MAX(\zeta_{TSI})$ indicator in Figure 11g-j. The process with largest, second and smallest contribution at any location can thus be directly identified from the corresponding color code. In the meantime, the area of one specific color represents the overall relative contribution in the whole PRE. Clearly no matter which intensity index is used, the results demonstrate a common conclusion that among all the largest contribution figures (a, d and g), the quadratic bottom friction occupies the largest area, which means the bottom friction contributes the most to the tide-surge interaction. In the second contribution figures (b, e and h), the shallow water effect is clearly the most significant and hence it contributes to the tide-surge interaction at the second level and nonlinear advection is the third significant contributor in the majority area of PRE as shown in c, f and j. Similar to that shown in Figure 10, the results obtained from I_r are close to that from $RMS(\zeta_{TSI})$ but are different from $MAX(\zeta_{TSI})$ at certain locations. For example, in the top of Shenzhen Bay, Figure 11d demonstrates that the shallow water effect dominates, whereas Figure 11g showes the quadratic bottom friction is more important. Due to its shallow water depth, this area is expected to be more significantly affected by the shallow water effect. Therefore, as demonstrated above, the I_r in Eq. (16) is recommended to use for the quantification of the contributions from any particular process.

6 SUMMARY AND CONCLUSIONS

451

452

453 454

455

456 457

458

459

460

461

462

463

464 465

466

467 468

469

470

471

472 473

474

475 476

477

478

479

480

481 482

483

484 485

486 487

488

489

In this study, the characteristics and mechanism of tide-surge interaction in the Pearl River Estuary during Typhoon Hato is studied in detail by using a 3D ocean model (Zheng et al., 2017b). Along with the use of a blended atmospheric forcing which merged the Holland parametric model results with the CFSR reanalysis

498 499

500

501

502

503

504

505 506

507

508 509

510

511

512

514

515

516

517

518

519 520

521

522523

524

525 526

527

528

529

530

531

532533

534

535

data, the model reproduces the pure astronomical tides and total seal levels reasonably well, especially at Guanchong and Xipaotai where the distinctive "double-peak" pattern observed in the measured water levels is well reproduced by the present model.

To study the characteristics of tide-surge interaction in the PRE, three types of model runs are conducted, from which the total water level (storm tide ζ_{ST}), the pure storm surge (ζ_{SO}), the pure astronomical tide level (ζ_{TO}) , the practical storm surge (ζ_{PS}) and the residual elevation due to the tide-surge interaction (ζ_{TSI}) are obtained. These results show that due to the tide-surge interaction, the storm surge is clearly modulated by the tide level, e.g. the magnitudes of ζ_{PS} are greater near low tide but smaller near high tide than ζ_{SO} . The timing of surge is also altered due to the tidal modulation effect, and the peaks of the predicted ζ_{PS} shown in Figure 6 arrive a bit earlier than that of ζ_{SO} . The horizontal distributions of the differences between ζ_{PS}^{max} and ζ_{SO}^{max} (and the differences between ζ_{ST}^{max} and $[\zeta_{SO}+\zeta_{TO}]^{max}$) show that the effect of tide-surge interaction can either enhance or reduce the peak surge elevations. In addition, the resulted phase alteration can also affect the peak total water elevations (ζ_{ST}). A close examination of Figure 7c indicates that the phase alteration largely increases the peak ζ_{ST} in the majority of the PRE. One of the most notable areas affected by such a process is near the top of Shenzhen Bay, where a maximum magnitude of 0.18 m is found. Three indicators are used to quantify the absolute intensity of tide-surge interaction, including the previous used MAX(ζ_{TSI}), RMS(ζ_{TSI}), and a newly proposed I_r which reflects the total relative intensity of tide-surge interaction to pure storm surge and pure astronomical tide. As I_r eliminates the dependence of the interaction intensity on the magnitude of surge height and tidal range, it is considered more appropriate to be used in quantifying the relative importance of different physical processes to the tide-surge interaction.

A widely used "subtraction" approach and a new proposed "addition" approach are adopted to separate the contributions of three nonlinear processes to tide-surge interaction and to quantify their relative significance, respectively. In the widely used "subtraction" approach, each of the three processes is removed or linearised from a standard model that includes all processes. The contribution from each specific process to the tide-surge interaction is quantified based on the reduction rate (R_o) of interaction intensity. However, results show that the R_o from the "subtraction" approach is greatly affected by the "rebalance" effect (Figure 9), thus it can not correctly represents the significance of its corresponding nonlinear process. An "addition" approach is therefore proposed by adding one of the three processes onto the baseline simulation that without any nonlinear effects. A new general ratio R_n is defined to quantify the contribution of each process, the value of which can be calculated from either one of those three representative indicators of tide-surge interaction intensity. The comparison of the magnitudes of R_n between those obtained from three reduced experiments clearly show that the quadratic bottom friction, shallow water effect and nonlinear advective effect have the largest, second and third largest contribution to the tide-surge interactions in the majority of the PRE, respectively. Among the three indicators that have been used to represent the intensity of tide-surge interaction, I_r is suggested to be more reasonably used to quantify the relative importance of the three nonlinear effects.

Taking Typhoon Hato as a case study, the present research reveals detailed characteristics of tide-surge interaction in the PRE. The present results is thought to be able to provide valuable information for the coastal defense management of different regions inside the PRE, although studies on more typhoon events may be needed. Furthermore, the mechanism of of tide-surge interaction is examined by using a new proposed "addition approach". This new approach is free of the trouble due to the "rebalance" effect and thus is recommended to be used in later similar studies and in the other regions of world.

7 APPENDIX: RECONSTRUCTION OF TYPHOON HATO WIND FIELD

To model the typhoon induced storm surge reasonably well, an accurate atmospheric forcing is critical. 536 The commonly used reanalysis datasets (e.g. the CFSR data) are known to under-estimate the wind 537 speeds near the tropical cyclone centres, thus corrections are needed (Carr and Elsberry, 1997; Pan et al., 538 2016; Shao et al., 2018). In contrast, various parametric tropical cyclone models have been proposed 539 to produce much more realistic air pressure and wind distributions near the tropical cyclone centres 540 (Fujita, 1952; Jelesnianski, 1966; Holland, 1980; Knaff et al., 2007). However, they also fail to reproduce 541 realistic wind characteristics at a greater distance from the tropical cyclone centre, because the complex 542 meteorological environments there are very likely controlled by some other weather systems. As a result, 543 blended atmospheric fields that combine the above two kinds of datasets have been widely used in previous 544 545 studies (Carr and Elsberry, 1997; Jiang et al., 2003; Pan et al., 2016; Zheng et al., 2017a; Shao et al., 2018). In the present study, we follow the approach proposed by Pan et al. (2016) to merge the parametric tropical 546 cyclone model results (Holland, 1980) with the CFSR reanalysis atmospheric data. 547

In this study, the final adopted parametric tropical cyclone wind profile is given in Eq. (17). Based on the Holland parametric model (Holland, 1980), it describes the wind field associated with an axis-symmetric and static tropical cyclone, at the same time it accounts for the friction induced inflow angle and the translation motion of tropical cyclone.

$$\mathbf{V}_{TC} = c_1 v_q \left[-\sin(\theta + \theta_{in})\mathbf{i} + \cos(\theta + \theta_{in})\mathbf{j} \right] + \mathbf{V}_t$$
 (17)

where **i** and **j** are the unit vectors in the x and y directions, respectively; c_1 is a correction coefficient ($c_1 = 0.7$ in this study), which is used to adjust the wind speed to the standard 10 m elevation above the sea surface; θ is the angle between the x-axis and the line connecting the computing point and tropical cyclone center; θ_{in} is the inflow angle which depicts the deflection of actual wind direction from the tangential direction of the concentric circles. It can be calculated as follows (Harper et al., 2001):

$$\theta_{in} = \begin{cases} 10 \frac{r}{R_{max}} & , r < R_{max} \\ 10 + 75 \left(\frac{r}{R_{max}} - 1\right) & , R_{max} \le r < 1.2 R_{max} \\ 25 & , r > 1.2 R_{max} \end{cases}$$
(18)

557 r is the distance to the TC center; R_{max} is the radius to the maximum wind speed, which is usually calculated by an empirical equation proposed by Graham and Nunn (1959):

$$R_{max} = 28.52 \tanh \left[0.0873(\varphi - 28) \right] + 12.22 \exp \left(\frac{p_c - p_e}{33.86} \right) + 0.2 |\mathbf{V}_t| + 37.22$$
 (19)

where φ is the latitude of the tropical cyclone center; p_c is central surface pressure of the tropical cyclone; and p_e is the ambient pressure. V_t is the tropical cyclone translation speed. It's magnitude weakens with the distance from the tropical cyclone center, which can be described by an exponential function (Jakobsen and Madsen, 2004; Miyazaki, 1977) as follows:

$$\mathbf{V}_t = \exp\left(\frac{-\pi r}{500000}\right) \mathbf{V}_{tc} \tag{20}$$

in which V_{tc} is translation speed of tropical cyclone center and can be calculate from the tropical cyclone best track dataset. v_q is the Holland parametric static tropical cyclone wind profile and given as follows: 564

$$v_g(r) = \left\{ \frac{B}{\rho_a} \left(\frac{R_{max}}{r} \right)^B \left(p_e - p_c \right) \exp \left[-\left(\frac{R_{max}}{r} \right)^B \right] + \left(\frac{rf}{2} \right)^2 \right\}^{1/2} - \frac{rf}{2}$$
 (21)

in which ρ_a is the density of air; f is the Coriolis parameter; B is the shape parameter and can be calculated 565 from the maximum wind speed (v_{max}) as follows: 566

$$B = \frac{v_{max}^2 \rho_a e}{p_e - p_c} \tag{22}$$

The parametric atmospheric pressure (in millibars) at the sea level is given as: 567

$$p_s = p_c + (p_e - p_c) \exp\left[-\left(\frac{R_{max}}{r}\right)^B\right]$$
 (23)

CONFLICT OF INTEREST STATEMENT

The authors declare that the research was conducted in the absence of any commercial or financial relationships that could be construed as a potential conflict of interest. 569

AUTHOR CONTRIBUTIONS

PZ took part in all processes in this research, including wrote out the first draft paper, model setup and 570 experiments design, model results analysis; he also proposed the new "addition" approach and the use of I_r 571 indicator to represent the tide-surge interaction after some inspiring discussions with ML. ML modified the 572 first draft paper from the very beginning to the end, helped PZ to design the model experiments and also 573 gave advices in drafting this paper. CW designed the right approach to reconstruct the Typhoon Hato wind 574 field by merging the CFSR winds and Holland parametric model results; CW also provided the observed 575 wind data at six stations and made a preliminary comparison between the reconstructed and observed 576 wind at six stations. JW and XC helped PZ to analyse the model results, they also made some very useful 577 modifications to the draft paper, which greatly improved the readability and completeness of draft. MDD 578 and PY helped PZ to create the model mesh grid and to determine the basic model configuration. JW and 579 ZH are the project co-PIs, they provided critical data and revision advices on the structure of the manuscript. 580 All the authors particiated in the revision of the manuscript. 581

FUNDING

- This research was supported by the National Key Research and Development Project (grant 582
- 2016YFC1401300), the Joint Research Projects NSFC (No. 51761135022)-NWO (No. ALWSD.2016.026)-583
- EPSRC (No. EP/R024537/1): Sustainable Deltas and the National Natural Science Foundation of China 584
- (No. 51609269). 585

ACKNOWLEDGMENTS

- 586 Computational support was provided by the Barkla High Performance Computer at University of Liverpool
- and the ARCHER UK National Supercomputing Service (http://www.archer.ac.uk).

DATA AVAILABILITY STATEMENT

- 588 The raw data supporting the conclusions of this manuscript will be made available by the authors, without
- 589 undue reservation, to any qualified researcher.

REFERENCES

- 590 Bernier, N. B. and Thompson, K. R. (2007). Tide-surge interaction off the east coast of canada and
- northeastern united states. *Journal of Geophysical Research: Oceans* 112. doi:10.1029/2006JC003793
- 592 Bertin, X., Bruneau, N., Breilh, J.-F., Fortunato, A. B., and Karpytchev, M. (2012). Importance of wave
- age and resonance in storm surges: The case xynthia, bay of biscay. Ocean Modelling 42, 16–30
- 594 Bobanović, J., Thompson, K. R., Desjardins, S., and Ritchie, H. (2006). Forecasting storm surges along the
- east coast of canada and the north-eastern united states: The storm of 21 january 2000. Atmosphere-Ocean
- 596 44, 151–161
- 597 Brown, J. M., Souza, A. J., and Wolf, J. (2010). An 11-year validation of wave-surge modelling in the irish
- sea, using a nested polcoms–wam modelling system. Ocean Modelling 33, 118–128
- 599 Carr, L. E. and Elsberry, R. L. (1997). Models of tropical cyclone wind distribution and beta-effect
- propagation for application to tropical cyclone track forecasting. *Monthly Weather Review* 125, 3190–
- 601 3209. doi:10.1175/1520-0493(1997)125(3190:MOTCWD)2.0.CO;2
- 602 Chen, C., Liu, H., and Beardsley, R. C. (2003). An unstructured grid, finite-volume, three-dimensional,
- primitive equations ocean model: application to coastal ocean and estuaries. *Journal of Atmospheric and*
- 604 Oceanic Technology 20, 159–186. doi:10.1175/1520-0426(2003)020(0159:AUGFVT)2.0.CO;2
- 605 Doodson, A. T. (1956). Tides and storm surges in a long uniform gulf. Proceedings of the Royal Society of
- 606 London. Series A. Mathematical and Physical Sciences 237, 325–343
- 607 Egbert, G. D. and Erofeeva, S. Y. (2002). Efficient inverse modeling of barotropic ocean tides. Journal of
- 608 Atmospheric and Oceanic Technology 19, 183–204. doi:10.1175/1520-0426(2002)019 \langle 0183:EIMOBO \rangle
- 609 2.0.CO;2
- 610 Fujita, T. (1952). Pressure distribution within typhoon. Geophys. Mag. 23, 437–451
- 611 Graber, H. C., Cardone, V. J., Jensen, R. E., Slinn, D. N., Hagen, S. C., Cox, A. T., et al. (2006). Coastal
- forecasts and storm surge predictions for tropical cyclones: A timely partnership program. *Oceanography*
- 613 19, 609–646
- 614 Graham, H. and Nunn, D. (1959). Meteorological conditions pertinent to standard project hurricane.
- 615 Atlantic and Gulf Coasts of United States. Weather Bureau, US Department of Commerce, Washington,
- 616 *DC*
- 617 Harper, B., Hardy, T., Mason, L., Bode, L., Young, I., and Nielsen, P. (2001). Queensland climate change
- and community vulnerability to tropical cyclones: Ocean hazards assessment-stage 1. Report prepared
- 619 by Systems Engineering Australia in conjunction with James Cook University Marine Modelling Unit,
- 620 Queensland Government, March
- 621 HKO (2017). Hong kong observatory: Tropical cyclones in 2017
- 622 Holland, G. J. (1980). An analytic model of the wind and pressure profiles in hurricanes. *Monthly weather*
- 623 review 108, 1212–1218

- Horsburgh, K. and Wilson, C. (2007). Tide-surge interaction and its role in the distribution of surge residuals in the north sea. *Journal of Geophysical Research: Oceans* 112
- 626 Jakobsen, F. and Madsen, H. (2004). Comparison and further development of parametric tropical cyclone
- 627 models for storm surge modelling. Journal of Wind Engineering and Industrial Aerodynamics 92,
- 628 375–391
- Jelesnianski, C. P. (1966). Numerical computations of storm surges without bottom stress. *Monthly Weather Review* 94, 379–394
- Jiang, S., Wu, G., Zhu, Y., and Wenyu, S. (2003). Numerical simulation of typhoon wind field on zhanjiang port [j]. *Marine Forecasts* 2
- 633 Knaff, J. A., Sampson, C. R., DeMaria, M., Marchok, T. P., Gross, J. M., and McAdie, C. J. (2007).
- Statistical tropical cyclone wind radii prediction using climatology and persistence. *Weather and Forecasting* 22, 781–791
- Large, W. and Pond, S. (1981). Open ocean momentum flux measurements in moderate to strong winds.
 Journal of physical oceanography 11, 324–336
- 638 Li, L., Yang, J., Lin, C.-Y., Chua, C. T., Wang, Y., Zhao, K., et al. (2018). Field survey of typhoon hato
- 639 (2017) and a comparison with storm surge modeling in macau. Natural Hazards and Earth System
- 640 Sciences 18, 3167–3178. doi:10.5194/nhess-18-3167-2018
- 641 [Dataset] Miyazaki, M. (1977). Marine physics
- Pan, Y., ping Chen, Y., xia Li, J., and lin Ding, X. (2016). Improvement of wind field hindcasts for tropical
- 643 cyclones. *Water Science and Engineering* 9, 58 66. doi:https://doi.org/10.1016/j.wse.2016.02.002
- Peng, M., Xie, L., and Pietrafesa, L. J. (2004). A numerical study of storm surge and inundation in the
- croatan–albemarle–pamlico estuary system. Estuarine, Coastal and Shelf Science 59, 121–137
- 646 Proudman, J. (1955). The propagation of tide and surge in an estuary. *Proceedings of the Royal Society of*
- 647 London. Series A. Mathematical and Physical Sciences 231, 8–24
- 648 Proudman, J. (1957). Oscillations of tide and surge in an estuary of finite length. Journal of Fluid
- 649 *Mechanics* 2, 371–382
- 650 Pugh, D. (1996). Tides, surges and mean sea-level (reprinted with corrections) (John Wiley & Sons Ltd)
- 651 Quinn, N., Atkinson, P. M., and Wells, N. C. (2012). Modelling of tide and surge elevations in the solent
- and surrounding waters: The importance of tide–surge interactions. *Estuarine, Coastal and Shelf Science*
- 653 112, 162–172
- Rego, J. L. and Li, C. (2010). Nonlinear terms in storm surge predictions: Effect of tide and shelf geometry
- with case study from hurricane rita. Journal of Geophysical Research: Oceans 115
- Rossiter, J. R. (1961). Interaction between tide and surge in the thames. *Geophysical Journal International*
- 657 6, 29–53
- 658 Shao, Z., Liang, B., Li, H., Wu, G., and Wu, Z. (2018). Blended wind fields for wave modeling of tropical
- 659 cyclones in the south china sea and east china sea. *Applied Ocean Research* 71, 20–33
- 660 Tang, Y. M., Sanderson, B., Holland, G., and Grimshaw, R. (1996). A numerical study of storm surges and
- tides, with application to the north queensland coast. *Journal of Physical Oceanography* 26, 2700–2711
- 662 Willmott, C. J. (1981). On the validation of models. *Physical geography* 2, 184–194
- Wolf, J. (1978). Interaction of tide and surge in a semi-infinite uniform channel with application to surge
- propagation down the east coast of britain. Applied Mathematical Model 2, 245–253. doi:10.1016/
- 665 0307-904X(78)90017-3
- 666 Wolf, J. (1981). Surge-tide interaction in the north sea and river thames. Floods due to high winds and
- 667 *tides* , 75–94

- 668 Wolf, J. (2009). Coastal flooding: impacts of coupled wave-surge-tide models. Natural Hazards 49,
- 669 241–260
- 670 Zhang, H., Cheng, W., Qiu, X., Feng, X., and Gong, W. (2017). Tide-surge interaction along the east coast
- of the leizhou peninsula, south china sea. *Continental Shelf Research* 142, 32–49
- 672 Zhang, W.-Z., Shi, F., Hong, H.-S., Shang, S.-P., and Kirby, J. T. (2010). Tide-surge interaction intensified
- by the taiwan strait. *Journal of Geophysical Research: Oceans* 115
- 674 Zheng, J., Wang, J., Zhou, C., Zhao, H., and Sang, S. (2017a). Numerical simulation of typhoon-induced
- storm surge along jiangsu coast, part ii: Calculation of storm surge. Water Science and Engineering 10,
- 676 8–16
- 277 Zheng, P., Li, M., van der Zanden, J., Wolf, J., Chen, X., and Wang, C. (2017b). A 3d unstructured grid
- 678 nearshore hydrodynamic model based on the vortex force formalism. *Ocean Modelling* 116, 48–69